Geosci. Model Dev. Discuss., 8, 2313–2367, 2015
www.geosci-model-dev-discuss.net/8/2313/2015/
doi:10.5194/gmdd-8-2313-2015

Geoscientific Model Development Discussions
Open Access

Development and application of the WRFPLUS-Chem online chemistry adjoint and WRFDA-Chem assimilation system

J. J. Guerrette and D. K. Henze

Department of Mechanical Engineering, University of Colorado, Boulder, CO, 80309, USA

Received: 26 January 2015 – Accepted: 10 February 2015 – Published: 27 February 2015

Correspondence to: J. J. Guerrette (jonathan.guerrette@colorado.edu)

Published by Copernicus Publications on behalf of the European Geosciences Union.

Abstract

Here we present the online meteorology and chemistry adjoint and tangent linear model, WRFPLUS-Chem, which incorporates modules to treat boundary layer mixing, emission, aging, dry deposition, and advection of black carbon aerosol. We also develop land surface and surface layer adjoints to account for coupling between radiation and vertical mixing. Model performance is verified against finite difference derivative approximations. A second order checkpointing scheme is created to reduce computational costs and enable simulations longer than six hours. The adjoint is coupled to WRFDA-Chem, in order to conduct a sensitivity study of anthropogenic and biomass burning sources throughout California during the 2008 Arctic Research of the Composition of the Troposphere from Aircraft and Satellites (ARCTAS) field campaign. A cost function weighting scheme was devised to increase adjoint sensitivity robustness in future inverse modeling studies. Results of the sensitivity study show that, for this domain and time period, anthropogenic emissions are over predicted, while wildfire emissions are under predicted. We consider the diurnal variation in emission sensitivities to determine at what time sources should be scaled up or down. Also, adjoint sensitivities for two choices of land surface model indicate that emission inversion results would be sensitive to forward model configuration. The tools described here are the first step in conducting four-dimensional variational data assimilation in a coupled meteorology-chemistry model, which will potentially provide new constraints on aerosol precursor emissions and their distributions. Such analyses will be invaluable to assessments of particulate matter health and climate impacts.

1 Introduction

Fine particulate matter impacts human health (Schwartz et al., 2007; Krewski et al., 2009) and climate (Myhre et al., 2013). Atmospheric climate forcing from aerosols is potentially large, but also highly uncertain owing to a complex spatial-temporal distribu-

GMDD
8, 2313–2367, 2015

tion of concentration, mixing state, and particle size for multiple species, each emitted from varying precursor sources, both anthropogenic and natural (Textor et al., 2006; Schulz et al., 2006). Depending on the species and quality of records, a nation's annual aerosol precursor and primary emissions have uncertainties anywhere between 7 % and a factor of four, with larger variation on seasonal to diurnal scales for particular sectors (Streets et al., 2003; Suutari et al., 2001). Over these shorter time scales, aerosols impact meteorology through the semi-direct (Hansen et al., 1997; Koch and Del Genio, 2010) and indirect (Twomey, 1977; Lohmann and Feichter, 2005) cloud effects, which are both dependent on aerosol vertical profiles (e.g., Samset et al., 2013) governed by mixing.

Atmospheric models are used to improve our understanding of aerosol sources, distributions, and processes. Online numerical weather prediction and chemistry (NWP-chemistry) models integrate dynamic and chemical equations simultaneously, whereas offline chemical transport models (CTMs) interpolate meteorological fields from 3 to 6 h reanalyses. Grell et al. (2004) showed that vertical mass transport of chemical tracers is highly sensitive to the choice of online vs. offline modeling methodologies due to variations in boundary layer mixing strength. Additionally, NWP-chemistry models account for moisture and temperature perturbations to dynamics due to aerosol microphysics and radiative forcing, while CTMs can not account for these feedbacks.

There are numerous online models with aerosol-meteorology feedbacks (e.g., WRF-Chem (Skamarock et al., 2008; Grell et al., 2005), COSMO-ART (Vogel et al., 2009), GEM-AQ (Kaminski et al., 2008), and IFS-MOZART (Kinnison et al., 2007; Flemming et al., 2009; Morcrette et al., 2009)). Better descriptions of sources, loss mechanisms, and vertical transport in coupled models are needed to increase accuracies in short-term climate modeling (Baklanov et al., 2014). To address this, chemical data assimilation can be used to improve short-term forecasts. In WRF, three-dimensional variational data assimilation (3D-Var) (Pagowski et al., 2010; Liu et al., 2011; Schwartz et al., 2012; Saide et al., 2012, 2013), ensemble Kalman filter (EnKF) (Pagowski and Grell, 2012), and hybrid approaches (Schwartz et al., 2014) have all been used to improve chemical

GMDD
8, 2313–2367, 2015

initial conditions. The limitation of these studies, using sequential methods, has been the decay of chemical concentrations back to the emissions-driven values following the characteristic loss rate of each species, necessitating periodic reinitialization with new observations. Using data assimilation solely to perturb initial conditions leaves behind underlying deficiencies in model description, emissions, or other input parameters.

In contrast to 3-D approaches, 4-D data assimilation attempts to minimize the discrepancy between model predicted values and observations at the same time observations are acquired. Variational 4-D data assimilation (4D-Var) requires an adjoint, which calculates the sensitivity of a model metric to all input parameters, such as resolved aerosol precursor emissions. Several offline CTMs already have adjoints for constraining aerosol and aerosol precursor emissions, including GEOS-Chem (Henze et al., 2007), STEM (Sandu et al., 2005; Hakami et al., 2005), CMAQ (Turner et al., 2015), GOCART (Dubovik et al., 2008), and LMDz (Huneeus et al., 2009). Inverse modeling has been used to constrain aerosol emissions with 4D-Var, but only in offline models (e.g., Hakami et al., 2005; Dubovik et al., 2008; Henze et al., 2009; Wang et al., 2012). In addition to inverse modeling, derivatives calculated from CTM adjoints have been used to analyze sensitivities of model estimates to emissions (e.g., Turner et al., 2012). Online chemical 4-D variational data assimilation (4D-Var) has been performed with the global IFS-MOZART model, although without two-way coupling, to improve aerosol (Benedetti et al., 2009) and gas-phase (Inness et al., 2013) initial conditions. To our knowledge, 4D-Var still has not been used in a regional NWP-chemistry model with online coupling to constrain aerosol precursor emissions or other important model parameters, such as vertical mixing coefficients.

Here we present the first such system, building on existing capabilities of the WRF data assimilation (WRFDA) framework. WRFDA includes both 3D-Var (Barker et al., 2004) and incremental 4D-Var (Barker et al., 2005; Huang et al., 2009) algorithms, which are designed for constraining meteorological initial conditions (e.g., wind fields, temperature, moisture). For WRFDA v3.2 and later, WRF-4-DVar requires calling the WRFPLUS forward (FWM), tangent linear (TLM) and adjoint (ADM) models. These

GMDD
8, 2313–2367, 2015

models include adiabatic WRF dynamics, along with simplified surface friction (i.e., boundary layer), cumulus, and microphysics packages (Zhang et al., 2013). Here we integrate aerosol chemistry and vertical mixing from WRF-Chem into WRFPLUS, including complementary TLM and ADM components. While existing CTMs are capable of aerosol emission inversions, this development promises to introduce new insights into meteorology-chemistry couplings. We apply this system to black carbon (BC) aerosol, because of its important implications for climate (Bond et al., 2013) and health (Grahame et al., 2014). Additionally, the widespread use and development of WRF furthers the potential for continued model improvement and a community of future users.

BC is emitted from incomplete combustion of fuels. Major anthropogenic sources include residential cookstoves in developing countries, open crop burning, diesel transportation, and coal power plants with poor emission controls. Wildfires, or biomass burning, are the largest natural source. The major limitations to devising accurate bottom-up emissions inventories are poor activity data in developing countries and difficulty parameterizing complex biomass burning sources. Even in developed countries, changing economic landscapes affect real year-to-year emissions. Black carbon (BC) is unique among atmospheric aerosols as being radiatively absorptive, relatively inert, primary emitted, and having potentially complex cloud interactions. BC is possibly the second most important human emitted pollutant in terms of climate forcing in the present-day atmosphere, with a net forcing of $+1.1\,\mathrm{W\,m^{-2}}$, but with 90 % uncertainty ($+0.17$ to $+2.1\,\mathrm{W\,m^{-2}}$) (Bond et al., 2013). Also, reductions in BC emissions have been shown to reduce fine particulate health impacts (e.g., Anenberg et al., 2011).

The new TLM and ADM – referred to collectively herein as "AD/TL models" – aerosol treatments lay the groundwork for constraining aerosol precursor emissions using 4D-Var in a NWP-chemistry model. In Sect. 2, we describe the WRFPLUS-Chem and WRFDA-Chem model architectures. In Sect. 3, we describe the construction and verification of the AD/TL models of specific WRF-Chem forward model components. In Sect. 4, we describe a special checkpointing scheme that enables adjoint and tangent linear simulations longer than 6 h which are required for accumulating sensitivities of

GMDD
8, 2313–2367, 2015

sparse chemical observations with respect to emissions. In Sect. 5, we demonstrate the capability of the adjoint model to calculate sensitivities of BC observation errors in WRFDA-Chem. Finally, we discuss future developments for WRFPLUS-Chem and WRFDA-Chem.

2 Methods

Creating the foundation for WRFDA-Chem required managing relationships between five related, but separate models. These include the (1) Weather Research and Forecast Model (WRF), (2) its "-Chem" variant, and the (3, 4) WRFPLUS AD/TL models. Finally, (5) WRFDA 4D-Var requires communication of critical namelist and state variables to the FWM, TLM, and ADM. Figure 1 shows the relationships between these different models, including all AD/TL code that was previously developed, and code that we have added, modified, or plan to add.

2.1 Forward model

For this work, we use WRF version 3.6. The WRFPLUS-Chem code repository (https://svn-wrf-model.cgd.ucar.edu/branches/WRFPLUSV3-Chem) contains the most current version. Interested users can contact NCAR to request user access to the code. WRF contains multiple non-hydrostatic dynamic cores and parameterization options for modeling unresolved physical processes. The FWM is identical in WRF and WRFPLUS, though typically only very simple unresolved physics are applied in WRFPLUS. In addition, WRF-Chem simulates the emission, deposition, transport, turbulent and cumulus mixing, wet scavenging, cloud interactions, and chemical transformation of trace gasses and aerosols. All of these processes are modeled at the same spatial and temporal resolution, which enables coupling WRF radiation and microphysics calculations directly with chemical processes.

GMDD
8, 2313–2367, 2015

The forward model configuration for which we have developed the corresponding TLM and ADM will be referred to as the "adjoint model configuration," because we use the same settings when running the adjoint. We use GOCART aerosols (chem_opt = 300), wherein the chem array has 19 aerosol (e.g., SO_2, sulfate, black carbon, dust, sea salt) and zero gas-phase members. This option includes bulk mass sulfate chemistry and black carbon oxidative aging. We employ combined local and non-local ACM2 PBL mixing (Pleim, 2007b, a), with surface interactions handled by the Pleim-Xiu (PX) LSM (Xiu and Pleim, 2001; Pleim and Xiu, 2003; Pleim and Gilliam, 2009) and surface layer (Pleim, 2006) mechanisms (all options seven). Soil moisture and temperature nudging are not used within the PXLSM. Prior to version 3.6, the WRF-Chem vertical mixing scheme solely carried out PBL mixing and dry deposition for chemical species. That vertical mixing depended on a (local) turbulent eddy mixing coefficient from a user-selected PBL scheme and a dry deposition velocity. There is new capability to calculate tracer turbulent mixing and dry deposition within the ACM2 subroutine itself, enabling non-local mixing. Trace gas and particle deposition velocities are calculated using characteristic resistances found using methods from Wesely (1989). Microphysics and radiation AD/TL models with aerosol feedbacks have not been incorporated into WRFPLUS-Chem yet. These crucial components will be partially adapted from previous work (e.g. Saide et al., 2012, 2013), while others still need to be developed. Both microphysics and radiation are turned off for Sect. 3.3 verification simulations. In order to ensure appropriate radiative fluxes at the land-air boundary, the GSFCSW and Goddard LW radiation compute ground-incident radiation for the Sect. 5 adjoint sensitivity demonstration. However, online coupling between radiation and chemical species is deactivated.

2.2 Incremental 4D-Var

WRFDA uses an incremental 4D-Var method (Courtier et al., 1994) for finding the minimum of the cost function, J, by adjusting control variables (CV), $\boldsymbol{x}$. As described by

GMDD
8, 2313–2367, 2015

Huang et al. (2009), the WRFDA cost function has three terms

$$J = J_\mathrm{b} + J_\mathrm{o} + J_\mathrm{c}, \tag{1}$$

where J_b, J_o, and J_c are the background, observation, and balancing cost functions, respectively. J_c is not relevant to the current work. The background and observation cost functions are

$$J_\mathrm{b} = \frac{1}{2}\left[\left(\boldsymbol{x}^n - \boldsymbol{x}^{n-1}\right) + \sum_{i=1}^{n-1}\left(\boldsymbol{x}^i - \boldsymbol{x}^{i-1}\right)\right]^\mathrm{T} \mathbf{B}^{-1} \left[\left(\boldsymbol{x}^n - \boldsymbol{x}^{n-1}\right) + \sum_{i=1}^{n-1}\left(\boldsymbol{x}^i - \boldsymbol{x}^{i-1}\right)\right] \tag{2a}$$

and

$$\begin{aligned} J_\mathrm{o} &= \frac{1}{2}\sum_{k=1}^{K}\left\{H_k\left[M_k\left(\boldsymbol{x}^n\right)\right] - \boldsymbol{y}_k\right\}^\mathrm{T}\mathbf{R}_k^{-1} \left\{H_k\left[M_k\left(\boldsymbol{x}^n\right)\right] - \boldsymbol{y}_k\right\} \\ &\approx \frac{1}{2}\sum_{k=1}^{K}\left[\mathbf{H}_k\mathbf{M}_k\left(\boldsymbol{x}^n - \boldsymbol{x}^{n-1}\right) - \boldsymbol{d}_k\right]^\mathrm{T}\mathbf{R}_k^{-1} \left[\mathbf{H}_k\mathbf{M}_k\left(\boldsymbol{x}^n - \boldsymbol{x}^{n-1}\right) - \boldsymbol{d}_k\right]. \end{aligned} \tag{2b}$$

The background cost function is a penalty term, which ensures the departure of the posterior, $\boldsymbol{x}^n$, from the prior, $\boldsymbol{x}^0 = \boldsymbol{x}^\mathrm{b}$, remains within the bounds justified by the background error covariance, $\mathbf{B}$. The observation cost function measures the distance between the 4D-Var model solution, $\boldsymbol{x}^n$, and the observations, $\boldsymbol{y}$. M and H are the nonlinear model and observation operators, while $\mathbf{M}$ and $\mathbf{H}$ are their linearized forms, or

GMDD
8, 2313–2367, 2015

tangent linear operators, used to propagate analysis increments $\boldsymbol{\delta x} = \boldsymbol{x}^n - \boldsymbol{x}^{n-1}$ from the earliest emission time to the kth observation. **R** is the observation error covariance matrix. The innovation,

$$\boldsymbol{d}_k = \boldsymbol{y}_k - H_k\left[M_k\left(\boldsymbol{x}^{n-1}\right)\right], \tag{3}$$

is the residual error between the real and modeled observations k at the end of 4D-Var iteration $n-1$. This notation slightly differs from Huang et al. (2009), who employed K observation windows, each containing multiple observations.

For each iteration of incremental 4D-Var, the model is linearized about a trajectory, which is a collection of stored values of all model state variables at all time steps within the assimilation window. This trajectory enables propagation of sensitivities forward and backward in time within the TLM and ADM. Each of these models are called in an inner loop to calculate the gradient of the observation cost function, $\nabla_{\boldsymbol{x}} J_{\mathrm{o}}$. An optimization algorithm uses the gradients to calculate optimal analysis increments to the CVs, which minimize the observation cost function. If the CVs, $\boldsymbol{x}^n$, depart too much from the initial guess for the current outer loop iteration, $\boldsymbol{x}^{n-1}$, the model must be relinearized about the new state, $\boldsymbol{x}^n$, using M. The purpose of the two-level optimization is that approximating M with **M** transforms the cost function from a nonlinear to a quadratic form, and guarantees a unique solution $\boldsymbol{x}^*$ to the minimization (Courtier et al., 1994). Refer to Huang et al. (2009) for more details on the WRFDA incremental method, including a full expression for $\nabla_{\boldsymbol{x}} J$ given by Eq. (7) of that article. The main purpose of this work is to introduce the AD/TL model components of WRFPLUS-Chem.

3 Tangent linear and adjoint model construction and verification

We have developed and tested adjoint and tangent linear code to represent aerosol-relevant processes in WRFPLUS-Chem. This development required a four step process:

GMDD
8, 2313–2367, 2015

1. Automatically differentiate specific WRF-Chem modules using TAPENADE (Hascoët and Pascual, 2013) version 3.6.

2. Verify standalone TLM and ADM derivatives against finite difference approximations; debug as necessary.

3. Incorporate code manually into WRFPLUS.

4. Repeat step 2 for fully integrated WRFPLUS-Chem model.

TAPENADE takes discrete Fortran or C source code as input, then generates either TLM or ADM code using a user-generated list of independent and dependent parameters. In addition to creating the differential code, TAPENADE reduces adjoint computational cost by eliminating unnecessary lines of code. Similar to Xiao et al. (2008) and Zhang et al. (2013), integrating the automatically differentiated adjoint code into WRFPLUS required significant manual intervention and debugging. Methods for constructing discrete adjoints are well-documented (Giering and Kaminski, 1998; Hascoët and Pascual, 2013). For the remainder of this section, we discuss the particular mechanisms for which we have created AD/TL models, and then we provide verification results for WRFPLUS-Chem.

3.1 Transport mechanisms

PBL physics and dry deposition in a column are handled by ACM2. The simple surface friction previously developed for WRFPLUS does not perform vertical mixing of tracers, which is a minimum requirement of any PBL scheme used in WRFPLUS-Chem. The ACM2 PBL depends on ground-atmosphere interactions that necessitate additional surface layer and land surface model (LSM) AD/TL code. For example, the ACM2 PBL scheme depends on the friction velocity U^* calculated in a surface layer scheme, which itself depends on wind speed, and the state variables u and v. ACM2 also depends on surface heat (HFX) and moisture (QFX) fluxes, which can be calculated within the surface layer or LSM code, but also depend on U^*. The dependence of HFX and

GMDD
8, 2313–2367, 2015

QFX on ground-incident shortwave radiation (GSW) is calculated in the LSM. GSW is calculated in the radiation scheme, and depends on the aerosol composition and atmospheric moisture phase and distribution. Because we have not developed radiation AD/TL code, this coupling is not represented in WRFPLUS-Chem yet. The dependencies themselves are illustrative of how ACM2, and indeed most any other PBL scheme available in WRF, is appropriate for representing chemistry-meteorology interactions critical to understanding short-term climate impacts from aerosols. ACM2 is compatible with the Monin-Obukhov and PX (options 91 and 7) surface layer options, as well as the SLAB and PX (options 1 and 7) LSM options. TLM and ADM code is developed for all of these choices, and have been tested in standalone verification tests. In the interest of brevity, complete model verification in Sect. 3.3 has been limited to the two PX options.

Advection of inert tracers was added to WRFPLUS by X. Zhang (2012, personal communication). The same treatment has been applied to the "chem" array, with additional checkpointing and parallel communications. We generated standalone TLM and ADM code for deep cumulus convection as handled by the Grell–Freitas cumulus scheme (Grell and Freitas, 2014). One of the major benefits of this cumulus scheme is the ability to use online calculated cloud condensation nuclei (CCN) to account for the effect of aerosols on liquid and vapor water mass fractions. These parameters directly impact convection, including tracer transport. The ability of the standalone AD/TL codes to produce the relevant members of the Jacobian has been verified for a single set of column conditions using similar methods as described in Sect. 3.3. However, the FWM, TLM, and ADM do not yet account for vertical transport of chemical tracers, and thus have not been integrated into WRFPLUS-Chem.

3.2 Aerosol-specific components

GOCART is a bulk aerosol scheme that treats reactive species (BC, OC, sulphate) using a total mass approach and divides non-reactive species (dust, sea salt) into multiple size bins (Chin et al., 2000). Oxidative aging for both BC and OC is handled

GMDD
8, 2313–2367, 2015

by a first-order decay from hydrophobic to hydrophilic forms using a time constant of 2.5 days. Sulphate (SO_4^{2-}) is produced from SO_2 and dimethyl sulfide precursor gases in GOCART. Sulphate chemistry also requires offline-calculated values for nitrate and OH radical, which are taken from climatologies available from the PREP-CHEM-SRC preprocessor (Freitas et al., 2011). WRFPLUS-Chem includes both the carbon and sulfate chemistry AD/TL codes, but only the BC component is tested and applied here.

Emissions of aerosol precursors in WRF-Chem is a linear process corresponding to specific chemistry and emission inventory options. Emission magnitudes are calculated, then distributed spatially and temporally, in offline preprocessors. Typically, emissions are read in hourly following some diurnal pattern. In order to make the emissions code easily differentiable, scaling factors are added to the emissions such that

$$\mathbf{E}_{c,i_{sc}} = \boldsymbol{\alpha}_{c,i_{sc}} \widetilde{\mathbf{E}}_c. \tag{4}$$

At any simulation time, $\widetilde{\mathbf{E}}_c$ are the emissions most recently read in from file for chemical species c. $\boldsymbol{\alpha}_{c,i_{sc}}$ and $\mathbf{E}_{c,i_{sc}}$ are the emission scaling factors and effective emissions, respectively, during scaling period i_{sc}. For emission inversions, the CVs, $\boldsymbol{x}$, are spatial-temporal resolved emission scaling factors. At the beginning of 4D-Var or during an adjoint sensitivity study, the scaling factors are set to unity. The scaling factors are applied in the FWM if environment option WRFPLUS == 1 is set during compilation.

Dry deposition velocities are calculated in WRF-Chem within the dry deposition driver. In order to ease adjoint code construction and reduce checkpointing requirements, the dry deposition velocity calculation is moved to immediately precede the PBL driver as depicted in Fig. 1. The new source code is similar to the dry deposition driver, except that only code corresponding to the GOCART aerosol option remains. The dry deposition AD/TL code accounts for dependencies of the dry deposition velocity on physical parameters (e.g., temperature, water vapor, U^*). As mentioned previously, the chemical concentrations are sensitive to dry deposition velocity within the PBL scheme.

GMDD
8, 2313–2367, 2015

3.3 Verification and linearity test

WRFPLUS FWM, TLM, and ADM performance were previously verified by Zhang et al. (2013). Here we use an alternative verification approach similar to that used by Henze et al. (2007). We use the TLM, ADM, and a centered finite difference approximation from the FWM to evaluate derivatives

$$\chi_{p,q} = \frac{\partial J_{p,f}}{\partial x_{q,0}}, \tag{5}$$

of some cost function at location p and time step f with respect to some CV at location q and the initial time 0. The finite difference derivatives are calculated from

$$\chi_{p,q}^{\mathrm{NL}} \approx \frac{J_{p,f}\left(x_{q,0}+\delta x\right) - J_p, f\left(x_{q,0}-\delta x\right)}{2\delta x}, \tag{6}$$

where each evaluation of J results from a FWM evaluation with some perturbed value of $x_{q,0}$. δx varies between 0.1 and 10 % of the value of $x_{q,0}$. The adjoint and tangent linear derivatives are found by forcing the model gradient fields, λ^* and λ, at J_p and x_q, respectively. The tangent linear gradient and adjoint gradient variables are analogous to state variables in the FWM. We force gradients of 1.0, indicating a 100 % perturbation of the variable, and the resulting derivatives are retrieved from the model output gradient fields, such that

$$\chi_{p,q}^{\mathrm{TL}} = \lambda_{p,f} = \mathbf{M}\left(\lambda_{q,0}\right) \tag{7}$$

and

$$\chi_{p,q}^{\mathrm{AD}} = \lambda_{q,0}^{*} = \mathbf{M}^{\mathrm{T}}\left(\lambda_{p,f}^{*}\right), \tag{8}$$

where $\mathbf{M}^{\mathrm{T}}$ is the adjoint operator.

GMDD
8, 2313–2367, 2015

In order to evaluate our additions to WRFPLUS-Chem, we test cost functions equal to hydrophobic (BC_1) and hydrophilic (BC_2) black carbon concentrations in 100 different grid cells. We evaluate derivatives with respect to five state variables at three initial locations for each of those 200 cost functions. The CVs include initial conditions for BC_1, U, T, and Q_v, and also BC emission scaling factors, α_{BC}. All sensitivities apply over a 3 h duration for a domain covering the southwest United States. For a full domain and model setup description refer to Sect. 5.1.1. Figure 2 shows that the maximum relative error between the TLM and ADM is in the 8th significant digit. Thus we only need to compare the nonlinear model to the TLM to verify both the TLM and ADM. Those results are given in Fig. 3. The slope and R^2 statistic for a linear fit of those comparisons are very nearly unity for all CVs tested. Each of the plots in Figs. 2 and 3 depicts 600 derivative evaluations. A range of finite difference perturbations δx is used for U, T, and Q_v control variables in order to find a value of χ^{NL} with the best compromise between truncation and roundoff error. We test derivatives with respect to meteorological variables in order to show the AD/TL models will be functional in a setting with coupled chemistry and physics. In such a system, the emissions will impact meteorology, which in turn impacts concentrations. These results illustrate the capability of the AD/TL models to represent the latter part of that relationship. All of the verification results apply to a three hour simulation period, but longer simulations are needed to calculate the average influence of emissions on the modeled state-space.

4 Second order checkpointing

As discussed in Sect. 2.2, the nonlinear model trajectory is an integral component for propagating gradients in the AD/TL models. As one might imagine, the trajectory contains a large amount of information. WRFPLUS stores the entire double precision trajectory in memory in order to eliminate expensive I/O time. This is very helpful with regards to storage, but presents a challenge in terms of memory. The system is designed for 6 h operational assimilation windows. In a typical WRFPLUS-Chem simu-

GMDD
8, 2313–2367, 2015

lation there are at least twenty-eight 3-dimensional state variables (8 physical, 1 to 3 moisture, and 19 GOCART species), and numerous other 2- and 1-dimensional state variables that must be included in the trajectory. For an illustrative domain, simulating 3 h with a 90 s time step (18 km resolution), 79 × 79 columns, 42 levels, and a 5 cell boundary width, the trajectory would require 1.46 GB per core on 64 cores. This final cost per core includes a 50 % storage growth per doubling of the number of cores. Because the trajectory is stored for all time steps, required memory scales linearly with simulation duration and the number of simulated chemical species. For multi-day and multi-week inversions, as is typical in non-operational chemical data assimilation, the memory requirements become impractical for most cluster computing systems.

To solve this problem we implement a second order checkpointing scheme that shares the storage burden between the hard disks and memory. In a standard WRF-PLUS adjoint simulation, the FWM is called first in order to calculate the trajectory. The FWM integrates the nonlinear equations from the initial to the final time, and stores the model trajectory at each time step. The ADM integrates the transpose of the linearized model equations backward in time, and at each time step reads the trajectory previously stored by the FWM. This process is depicted as "1st-order checkpoint" in Fig. 4. Since the storage limitation is driven by the duration of a simulation, we break the simulation into smaller segments, while maintaining continuity in the adjoint derivatives. The checkpointed adjoint simulation begins with a full FWM simulation beginning at the initial time, t_0, and ending at the final time, t_f. WRF restart files are written at time intervals equal to the checkpoint interval, Δt_c. Once the simulation is completed, the FWM is restarted at initial time equal to $t_f - \Delta t_c$. During that simulation, the trajectory is stored in memory. The trajectory is then recalled in an adjoint simulation that proceeds backward toward the current initial time. The checkpoint system alternately calls the FWM and ADM until returning to t_0. The major hurdle to integrating this second order checkpointing system into WRF-4-DVar is that the trajectory is no longer readily available to WRFDA for calculating modeled observations, $H_k\left[M_k\left(\boldsymbol{x}^n\right)\right]$, between the calls to the forward and adjoint models. Instead, these values must be calculated during ei-

GMDD
8, 2313–2367, 2015

ther the full FWM (Step 1) or checkpoint FWM (Steps 2, 4, 6, etc.) simulations. We take the former approach. A similar checkpointing system is also implemented for the TLM in order to enable long duration incremental 4D-Var.

In order to ensure the checkpointing method delivers consistent derivatives to the non-checkpointed version, we again compare AD/TL derivatives to finite difference approximations. Because of the wall time required to calculate derivatives across extended time periods, we limit our tests to fourteen pairs of initial and final locations, q and p. For all of the J and x pairs tested in Sect. 3.3, the ADM and TLM agree to 13 or more digits over a 9 h test. The improved performance relative to the previous 3 h test came about after a few minor bug fixes. Because of this machine precision AD/TL agreement, we only compare the finite difference approximations to the TLM. For these checkpointed simulations, we analyze the derivative of a time variant cost function with respect to multiple control variables

$$\chi_{p,q}(t) = \frac{\partial J_p(t)}{\partial x_{q,0}}. \tag{9}$$

Doing so ensures that the derivatives are continuous across multiple checkpoint intervals and we are able to see the transient behavior of multiple finite difference perturbation sizes at times when there are large discrepancies with the TLM. The finite difference approximations of derivatives of BC with respect to the physical variables grow more unstable with time. Thus, we calculate those derivatives only for a 6 h period, while we test derivatives with respect to emissions for 48 h. Here we also include derivatives of U, T and Q_v with respect to U and Q_v to ensure that those relationships are represented properly in the surface layer, LSM, and PBL AD/TL schemes, so that they may be used in a meteorological 4D-Var setting.

Figure 5 shows the resulting derivatives for nine different pairs of J and x for a single pair of q and p. Most importantly for multi-day 4D-Var emissions inversions, BC concentrations respond linearly to a 1 % perturbation of emissions for at least 48 h. Next, it becomes apparent why derivatives with respect to U and Q_v require multiple finite dif-

GMDD
8, 2313–2367, 2015

ference perturbation sizes to ensure one of them matches the TLM at a particular cost function evaluation time. There are times when either the smallest, largest, or no value for δx agrees with the TLM. However, the TLM has inflection points at the same times as the finite difference approximations, including during periods of intense oscillation, such as for $\frac{\partial U}{\partial U}$ and $\frac{\partial U}{\partial Q_v}$. The chemical concentrations respond nonlinearly to all U and Q_v perturbation sizes for periods longer than 1 h in the plots shown, and longer than 3 h for all test scenarios considered. Further testing of these coupled derivatives will be necessary to determine over what time period they are suitable for inverse modeling, and under what conditions the model nonlinearities cease to be a limiting factor. Future emission inversion work with coupled physics and chemistry will need to verify that $\frac{\partial J}{\partial \alpha}$ has a near linear response over the time frame considered. The behaviors noted here are consistent across the other thirteen pairs of q and p.

5 Sensitivities to BC emissions in California

Here we demonstrate the new WRFPLUS-Chem capabilities in an adjoint sensitivity study. For the present example, the 4D-Var cost function is the model response metric and the biomass burning, and weekday and weekend anthropogenic emissions are the model parameters of interest. This framework is used to analyze where and when these parameters most impact the model performance and are thus in need of improvement.

5.1 Approach

For this demonstration, we calculate the sensitivity of the 4D-Var cost function in the first iteration. The background term is zero and there has been no prior CV increment (i.e., $\boldsymbol{\delta x} = \mathbf{0}$). Therefore, the cost function, Eq. (1), simplifies to

$$J = \frac{1}{2} \sum_{k=1}^{K} \{H_k \left[M_k(\boldsymbol{x}_b)\right] - \boldsymbol{y}_k\}^{\mathrm{T}} \mathbf{R}_k^{-1}$$

GMDD
8, 2313–2367, 2015

$$\{H_k\left[M_k(\boldsymbol{x}_b)\right]-\boldsymbol{y}_k\}. \tag{10}$$

All off-diagonal covariances in **R** are assumed to be zero in order to enable timely matrix inversion.

5.1.1 Model configuration

The model domain encompasses California and other southwest US states from 20 June 2008, 00:00:00 UTC to 27 June 2008, 09:00:00 UTC. We generated chemical initial conditions by running WRF-Chem for five days prior to the adjoint time period. We used the default WRF-Chem boundary condition for BC concentration of 0.02 $\mu g\,kg^{-1}$. This is consistent with a single upwind Pacific ocean transect taken during the 22 June flight. Meteorological initial and boundary conditions are interpolated from 3 h, 32 km North American Regional Reanalysis (NARR) fields. The horizontal resolution is 18 km throughout, and there are 42 vertical levels between the surface and model top at 100 hPa. The eta levels are 1.000, 0.997, 0.993, 0.987, 0.977, 0.967, 0.957, 0.946, 0.934, 0.921, 0.908, 0.894, 0.880, 0.860, 0.840, 0.820, 0.800, 0.780, 0.750, 0.720, 0.690, 0.660, 0.620, 0.570, 0.520, 0.470, 0.430, 0.390, 0.350, 0.310, 0.270, 0.230, 0.190, 0.150, 0.115, 0.090 , 0.07 , 0.052, 0.035, 0.020, 0.010, and 0.000. For a column where the ground is at sea level, there are 13 levels below 1 km and an additional 5 levels below 2 km. The subgrid physics options used are described in Sect. 2.1.

Anthropogenic emissions are taken from the US EPA's 2005 National Emissions Inventory (NEI2005). Fire emissions are provided by the Fire INventory from NCAR (FINN Version 1) (Wiedinmyer et al., 2011, 2006). FINN uses Moderate Resolution Imaging Spectroradiometer (MODIS) active fire locations and radiative power from NASA Terra and Aqua satellites, as well as speciated emission factors for four vegetation types, to calculate daily total 1 km resolution emissions. Burned areas are scaled to the combined fractional coverage of each 1 km^2 fire pixel by tree and herbaceous vegetation types assigned by the MODIS Vegetation Continuous Fields product (Hansen et al., 2003). Repeated fire detections in a single fire pixel are removed according to

GMDD
8, 2313–2367, 2015

Al-Saadi et al. (2008). Plume rise injection heights are calculated in WRF-Chem by an embedded one-dimensional cloud-resolving model (Freitas et al., 2007, 2010; Grell et al., 2011).

5.1.2 Model-observation comparison

We compare the model to observations in individual time steps, which differs from previous data assimilation approaches with WRF. In the standard WRFDA 4D-Var architecture, observations are binned over intervals, or windows, typically of one hour or longer duration. Whereas WRFDA typically has k observation windows, here WRFDA-Chem and WRFPLUS-Chem handle k observations possibly each at a different time. In order to reduce memory requirements, the adjoint forcing is stored in a column array, instead of the 2-D and 3-D arrays that were required for each state variable for each window, k in WRFDA. Also, while WRFDA includes meteorological observation operators to be called offline, a fine temporal resolution observation operator must be called directly within WRFPLUS. The traditional approach made communication between WRFDA and WRFPLUS less cumbersome, but also limited the ability to use dynamic observations recorded across broad temporal scales in an inversion.

In-situ observations were collected throughout California during the June 2008 portion of the Arctic Research of the Composition of the Troposphere from Aircraft and Satellites field campaign in collaboration with the California Air Resources Board (ARCTAS-CARB) (Jacob et al., 2009). Instruments aboard the DC-8 aircraft measured trace gas and aerosol concentrations over four days, including elemental carbon (EC) from the single particle soot photometer (SP2) at 10 s intervals (Sahu et al., 2012). Additionally, 41 Interagency Monitoring of Protected Visual Environments (IMPROVE) sites measured daily average surface light absorbing carbon (LAC) on 20, 23, and 26 June by thermal/optical reflectance (TOR) analysis of quartz filters (Malm et al., 1994). Surface and aircraft observation locations during the campaign are indicated in Figs. 6 and 7. The aircraft trajectories are overlaid on MODIS Aqua true color images (Gumley, 2008), and locations of MODIS active fires ().

GMDD
8, 2313–2367, 2015

The observation operators for aircraft and surface observations require temporal averaging. The 10 s resolution ARCTAS observations of BC concentration, pressure, latitude, and longitude are averaged to the 90 s model time step, which is approximately the time the DC-8 would take to traverse a single 18 km × 18 km column. However, the 10 s resolution ARCTAS BC concentrations are revision 2 (R2), while a later revision 3 (R3) product was released at 60 s resolution only. The later revision includes additional mass in the 50–900 nm size range as a result of applying a lognormal fit. In order to utilize this improved product, as well as leverage the finer resolution observations, the 10 s BC mass is scaled by the mass ratio between the 60 s R3 and the 60 s average R2 datasets. The scaled 90 s average observations are compared directly with the nearest model grid cell so that the model values are not interpolated. The pressure measurements are compared to online model pressures to determine the model level of each observation. For 24 h average surface measurements from IMPROVE, the observation operator averages the nearest model surface grid cell concentration over all time steps within the observation period. For the few surface sites that have two air samplers simultaneously measuring, they are averaged together to prevent nonzero correlation in the cost function (i.e., off-diagonal terms in **R**). After all averaging, there are 995 aircraft observations and 107 surface observations.

As depicted in Fig. 8, the WRF-Chem simulation is, on average, biased low for both the surface and aircraft observations. The lowest biased aircraft observations tend to be at higher altitudes, although this is not true in all cases. There are many high biased observations, and they tend to be at lower altitudes and to occur earlier in the simulation period when anthropogenic emissions dominate. Both surface and aircraft model predictions exhibit a wide spread of positive and negative errors. In order to determine potential causes for bias in specific locations, we consider the model residual errors, or simply "residuals,"

$$r_k = H_k \left[M_k \left(\boldsymbol{x}_b \right) \right] - \boldsymbol{y}_k, \tag{11}$$

GMDD
8, 2313–2367, 2015

for each aircraft observation k. Figure 7 shows the statistically significant ($p < 0.32$) residuals for observations above and below the top of the model PBL. Section 5.1.3 describes relevant measures of observation variance and statistical significance.

Negative residuals, and hence low model bias, are most prevalent in northern California on 22 and 26 June, most likely due to under prediction of biomass burning sources. There is also low bias above the PBL in the southern San Joaquin Valley on 20 June and below the PBL inland from San Diego on 24 June. Although neither case has visual smoke in the MODIS images, there were fires detected within 300 km. The largest positive residual occurs in Palmdale, CA close to landing on 24 June. It could be indicative of either an emission error or the coarse horizontal resolution that collocates the airport with other significant nearby sources. Other notable high model biases aloft occur near cities during the flights on 20, 22, and 24 June. Similarly, surface site biases are higher near cities, and along the coast. As might be expected, proximity to sources is a strong indicator of error magnitude, as that is where the highest concentrations occur. The error sign appears to be consistent above and below the PBL where such observations are collocated. Still, the spatial error pattern could reflect some combination of meteorology and emissions deficiencies. For the positive residuals off the coast of Los Angeles on 22 and 24 June, there could be errors in predicting vertical mixing associated with the land-sea circulation or predominant near-surface wind direction. Discerning errors caused by emissions from those caused by meteorological mechanisms would require a separate in-depth study.

5.1.3 Variance and residual error significance

When **R** is assumed to be diagonal, each residual in the 4D-Var cost function is weighted inversely proportional to the observation error variance. The form of the cost function is based in Bayesian statistics, with an aim of converging on posterior control variables in a maximum-likelihood sense. However, using the variance alone to weight the residuals may result in very large cost function terms for relatively small residual errors. As our interest in this study is to determine how errors in emission estimates

GMDD
8, 2313–2367, 2015

may be leading to model bias, we wish to ensure the largest residuals have the greatest weight, while also accounting for differences in statistical significance of particular errors. Thus we define the diagonal terms of **R** as

$$R_{k,k} = \frac{w_k}{\sigma^2_{k,k}}, \tag{12}$$

where w_k is an additional weighting term and $\sigma^2_{k,k}$ is the variance.

The variance is comprised of components due to both observation and model uncertainty as

$$\sigma^2_{k,k} = \sigma^2_k = \sigma^2_{k,m} + \sigma^2_{k,o}. \tag{13}$$

The model variance at each observation location is found from an ensemble of N_c = 156 WRF-Chem configurations during the modeling period. Each ensemble member, c, uses a different combination of PBL, surface layer, LSM, and longwave and shortwave radiation options. Also, there are configurations both with and without microphysics and cumulus convection. From the ensemble, we use the population of residuals at each observation, k, to calculate the model variance

$$\sigma^2_{k,m} = \mathrm{MAX}\left(\sum_{c=1}^{N_c} \frac{(r_{k,c})^2}{N_c - 1}, \mathrm{MML}^2\right), \tag{14}$$

where MML is the minimum model limit. The minimum possible modeled BC concentration is limited by the boundary condition, which fills the entire model domain during the five day warm-up simulation. The MML is simply taken as the minimum model concentration for all observation locations and all model configurations, and is found to be 0.01 and 0.02 $\mu g\,m^{-3}$ for aircraft and surface measurements, respectively, after rounding to the observation precision.

GMDD
8, 2313–2367, 2015

The IMPROVE instrument variance combines both relative and absolute uncertainties, the latter of which arises due to the minimum detection limit (MDL) (UC-Davis, 2002). For a single filter analysis, the variance (in $\mu g^2\,m^{-6}$) is

$$\sigma^2_{l_k,\text{inst.}} = \left[\frac{\sqrt{34^2 + \left[(1000)(0.07)\,y_{l_k}\right]^2}}{1000}\right]^2 . \tag{15}$$

The sub-observation index l_k is useful at sites with more than one air sampler. When a site has data from multiple instruments in a single day, we take their average and combine their instrument variances as

$$\sigma^2_{k,o} = \sum_{l_k}^{L_k} \frac{\sigma^2_{l_k,\text{inst.}}}{L_k^2}, \tag{16}$$

where L_k is the observation count. We assume the IMPROVE measurements fully represent the encompassing grid cell, since all sites are in remote locations and the samples are averaged over a 24 h period.

In contrast, the aircraft variance must capture the representativeness uncertainty associated with comparing the average of an entire model grid cell with an average of multiple short duration segments of a sparse aircraft transect. According to commercial literature for the SP2 device, it has an MDL of 0.01 $\mu g\,m^{-3}$, which we assume applies over the 10 s observation interval used during the ARCTAS campaign. The observations available through the NASA ARCTAS data archive have a BC mass concentration uncertainty of ±30 %. Although Sahu et al. (2012) report ±10 % BC mass uncertainty, that range is given by Kondo et al. (2011), who state their results are applicable in regions not impacted by refractory organic compounds, such as from biomass burning sources. Because there are significant burning sources in this domain, we adopt the

GMDD
8, 2313–2367, 2015

more conservative range. We utilize the instrument uncertainties in a definition for total observation variance with components due to both averaging and representativeness, such that for each average aircraft measurement,

$$\bar{y}_k = \sum_{l_k=1}^{L_k} \frac{y_{l_k}}{L_k}, \tag{17}$$

the total variance is

$$\sigma_{k,o}^2 = \mathrm{MDL}^2 + \sigma_{k,\mathrm{avg.}}^2 + \sigma_{k,\mathrm{rep.}}^2. \tag{18}$$

Adding the minimum variance associated with the MDL prevents the total variance from trending toward zero for any particular observation. This is important when using the variance in the cost function to ensure that near zero observations – which have low variances – with small residuals do not dominate the inversion. The averaging variance is the variance of the y_{l_k}'s that makeup $\bar{y}_k$, which is an attempt to capture the spread of true concentrations in a model grid cell. In the case that there is only a single observation, the averaging uncertainty is taken as double the instrument uncertainty. Thus,

$$\sigma_{k,\mathrm{avg.}}^2 = \begin{cases} \sum_{l_k=1}^{L_k} \left[\frac{\left(y_{l_k} - \bar{y}_k\right)^2}{L_k - 1} \right] & \text{if } L_k > 1; \\ \left(2\sigma_{k,\mathrm{inst.}}\right)^2 & \text{if } L_k = 1 \end{cases} \tag{19}$$

For any time step where $L_k < L_{\max} = 9$, there is an additional variance penalty proportional to the sum of the individual instrument variances,

$$\sigma_{k,\mathrm{rep.}}^2 = \sqrt{\frac{L_{\max} - L_k}{L_{\max}}} \sum_{l_k=1}^{L_k} \frac{\sigma_{l_k,\mathrm{inst.}}^2}{L_k^2}, \tag{20}$$

GMDD
8, 2313–2367, 2015

where

$$\sigma_{l_k,\text{inst.}} = \text{MAX}\left(\text{MDL}, 0.3 \cdot y_{l_k}\right). \tag{21}$$

In order to motivate the weight, w_k, applied to each residual model error, let us consider the primary inputs to the adjoint simulation, which are the adjoint forcings

$$\begin{aligned} \lambda^*_{k,m} &= \frac{\partial J}{\partial c_k} \\ &= \mathbf{H}_k^{\mathsf{T}} \sigma_k^{-2} \{H_k \left[M_k(\boldsymbol{x}_b)\right] - \boldsymbol{y}_k\} \\ &= \mathbf{H}_k^{\mathsf{T}} \lambda^*_{k,o}. \end{aligned} \tag{22}$$

c_k is any state variable on which H_k depends and which $M_k(\boldsymbol{x}_b)$ predicts. For our purposes, the state variables are modeled BC concentrations. The adjoint of the observation operator, $\mathbf{H}_k^{\mathsf{T}}$ transforms the forcing from observation space ($\lambda^*_{k,o}$) back to model space ($\lambda^*_{k,m}$). Thus, the forcing in observation space is

$$\lambda^*_{k,o} = \frac{r_k}{\sigma_k^2}. \tag{23}$$

Observations with significant model bias would require the largest perturbation in control variables to alleviate, and would seem to inform the inversion process the greatest. However, they must also have low total variance to contribute to an inversion. Figure 9 shows the surface and aircraft SD plotted vs. residual error. Also plotted in that figure are one and two SD zones, as well as lines of constant $\lambda^*_{k,o}$ for all $w_k = 1$. Any residual falling outside the 2σ zone is one where the combined model and observation SD is small enough to say with 95 % confidence ($p < 0.05$) that the residual error deviates from zero (i.e., the model and observation disagree). These statistically significant model errors indicate that some kind of inversion is worthwhile. The relative

GMDD
8, 2313–2367, 2015

contributions of observation and model variances is in general proportional to the relative magnitudes of observed and modeled concentration. Thus, model (observation) variation contributes to a large fraction of uncertainty in positive (negative) residuals.

There are several outlier negative residuals with magnitudes much larger than the remainder of the population. A large portion of these have large enough uncertainty that their adjoint forcing is much less than that of other lower magnitude residuals. Consider the region where $|r_k| < 0.5\,\mu g\,m^{-3}$ and $\sigma_k < 0.3\,\mu g\,m^{-3}$. The adjoint forcing magnitude is between 10 and $200\,\mu g^{-1} m^3$, varying the mean forcing magnitude to the maximum for any observation in the whole population. The residual errors within the 1σ and 2σ zones are not statistically significant, yet they might have larger adjoint forcing than observations with larger residual error at higher significance levels. Applying these adjoint forcings as-is could drive the inversion to fitting data points with small absolute residual error. This adjoint forcing imbalance between high and low significance observations can be alleviated by a counteracting weighting scheme. In order to devise such a scheme, we consider which forms of statistical significance are important to this inverse problem.

Because our goal in an emission inversion is to reduce model bias by perturbing emissions, model bias is itself an important characteristic. We use the ensemble of model configurations to calculate the variance in all residual errors, that is

$$\sigma_r^2 = \sum_{c=1}^{N_c} \sum_{k=1}^{K} \frac{r_{k,c}^2}{N_c K - 1}. \tag{24}$$

The residual SD, σ_r, are 0.69 and $0.29\,\mu g\,m^{-3}$ for surface and aircraft observation populations, respectively. After confirming that the residual errors are approximately normally distributed, the significance of the bias of a single observation relative to the

GMDD
8, 2313–2367, 2015

entire population is

$$f_{\mathrm{POP},k} = \mathrm{erf}\left(\frac{|\widetilde{r}_k|}{\sqrt{2\sigma_{\mathrm{r}}^2}}\right). \tag{25}$$

In statistics, the ratio of $\frac{|\widetilde{r}_k|}{\sigma_{\mathrm{r}}}$ is called the z value, and denotes the number of SD between $\widetilde{r}_k$ and the expected value of zero. The variable $\widetilde{r}_k$ indicates the user must select a specific form of residual error. Two examples are the mean or median of r_k. A third approach, and the one taken here is to use the residual found in the first 4D-Var iteration, $r_{k,n=0}$. $f_{\mathrm{POP},k}$ is a continuously variable p value, or the percentage of the population of all $r_{k,c}$ that is less significant than $\widetilde{r}_k$. Another measure of significance is visualized in the σ zones of Fig. 9, and was discussed previously. That is, for an individual residual error and variance, what is the probability that there will always be mismatch between the model and observation? The individual error significance is

$$f_{\mathrm{IND},k} = \mathrm{erf}\left(\frac{|\widetilde{r}_k|}{\sqrt{2\sigma_k^2}}\right). \tag{26}$$

The population and individual error significances are combined to derive the adjoint forcing weight,

$$w_k = \left[\left(f_{\mathrm{POP},k}\right)^{\gamma}\left(f_{\mathrm{IND},k}\right)^{1-\gamma}\right]^{\beta}. \tag{27}$$

The weighting scheme can be tuned for a specific application using the γ and β parameters to reshape the adjoint forcing contours. However, care must be taken when selecting γ, β, and $\widetilde{r}_k$ to ensure convergence in 4D-Var to the mean of the Gaussian distribution of residual errors. Here we only introduce the weighting scheme and use

GMDD
8, 2313–2367, 2015

it in a demonstration, but do not verify its validity. We use $\gamma = 0.5$ to provide some balance between the two measures of significance and $\beta = 2$ to ensure the weighting has a large impact. After calculating the w_k's according to Eq. (27), the new effective adjoint forcings are compared to the original values in Fig. 10. The weighting scheme is successful at reducing the impact of observation errors with low significance on the cost function.

After applying the new weighting scheme, the $\lambda^*_{k,o}$ contours no longer converge on the y axis as depicted in Fig. 9. Instead, they exit radially from the origin in all directions. As both the population and individual z values approach zero, the adjoint forcing converges toward

$$\lambda^*_{k,o} \approx \frac{r_k}{\sigma_k^2}\left(0.8\frac{|\widetilde{r}_k|}{\sigma_r^{\gamma}\sigma_k^{1-\gamma}}\right)^{\beta} = 0.64\frac{r_k\widetilde{r}_k^2}{\sigma_r\sigma_k^3}. \tag{28}$$

For our specific values of σ_r, all residual errors within the 2σ zone satisfy $|\lambda^*_{k,o}| \lesssim 5\,\mu g^{-1}m^3$ for surface, and $|\lambda^*_{k,o}| \lesssim 10\,\mu g^{-1}m^3$ for aircraft observations.

5.2 Results and discussion

With the weighting function applied, we calculate sensitivities of the 4D-Var cost function with respect to emissions for determining potential sources of model bias. The weights reduce the cost function from 5374 to 3784, which increases the normalized cost function sensitivity to emission perturbations. Figure 11 shows fully normalized sensitivities,

$$\frac{\partial \ln J}{\partial \ln E_{i,j,d}} = \sum_{n=1}^{24} \frac{\partial \ln J}{\partial \ln E_{i,j,d,n}}, \tag{29}$$

for six days of the simulation. The sensitivity in a particular grid cell is summed over the local diurnal cycle for hours $n = [1,\ldots,24]$ on day d. For anthropogenic emissions,

GMDD
8, 2313–2367, 2015

the local time is calculated for discrete 15° time zones, whereas for biomass burning emissions, local time corresponds to the continuous sun cycle. Undoubtedly, there are locations with positive and negative sensitivities at different times of day that will cancel, but this temporally aggregated sensitivity is an attempt to obtain average daily relationships across the domain. Although the color bar has been saturated at $\pm 5 \times 10^{-3}$, the full range of sensitivities are from -2.7×10^{-3} to $+5.6 \times 10^{-3}$ and -5.4×10^{-3} to $+6.3 \times 10^{-3}$ for anthropogenic and biomass burning emissions, respectively.

The magnitude of a normalized sensitivity corresponds to the fractional response in the cost function given a 100 % perturbation of emissions in a grid cell. If the model were perfect, the sensitivity magnitudes would be proportional to the difference between the background emission estimate and the true value. Thus a negative sensitivity indicates a location where estimated sources are too low, and vice versa. Because the sensitivities themselves depend on the emission magnitudes, they will change in each 4D-Var iteration, eventually converging on a minimum of the cost function where the sensitivities are zero. We use the sensitivities here as a qualitative indicator of emission errors, and not a quantitative conclusion as might be provided with a complete inversion.

The sensitivities exhibit a similar spatial-temporal pattern as the residual errors in Figs. 6 and 7, in general indicating that estimated anthropogenic emissions are too high, and that estimated fire emissions are too low. A more complex depiction of all BC emission errors arises in the sensitivities than the residuals alone might reveal. While most non-negligible burning sensitivities are negative, emissions from the Los Padres National Forest and northern redwoods on 23 June are potentially too high. The relative contributions of those fire estimates and simultaneous anthropogenic sources to positive coastal surface residuals near L.A. on 23 June are difficult to disentangle. However, the 24 June positive residuals from ARCTAS are more likely due to the anthropogenic sources. That is because the model transports smoke into the flight path of the DC-8 south of San Pedro, where BC concentrations are under predicted. Still, some anthropogenic source regions are under predicted as well.

GMDD
8, 2313–2367, 2015

The spatial variations in sensitivities are indicative of two phenomena. First, appreciable sensitivities will only arise in emissions that influence the particular observations available. Thus, full observation coverage is imperative to a successful inversion. Second, emission errors are heterogeneous in space and time. For biomass burning sources, heterogeneity arises due to missed detections in the MODIS active fire product, as well as potential errors in vegetation classification or attribution of a particular vegetation class to one of four land cover types used in FINN. Anthropogenic source error heterogeneity could be due to a static inventory from 2005 being used to describe emissions in 2008, or to spatial variations in BC emission factors for a particular source sector.

Comparative adjoint sensitivities are calculated using the SLAB LSM scheme (option 1) in place of the PX option. In these results, the same positive coastal sensitivities are even more pronounced and widespread on 23 and 24 June. Negative sensitivities to fires in the Sequoia and Inyo National Forests are larger in magnitude than those in the Sierras on 23 June, but the spatial sensitivity patterns between SLAB and PX options are consistent on 25 June. The differences are presumably due to changes in the residual error between the two configurations, since the weights and variances used are identical. $\tilde{r}_k$ was not recalculated for the SLAB case. The differing spatial sensitivity patterns indicate that the surface heat and moisture fluxes calculated by each LSM scheme contributes non-negligibly to the vertical mixing of BC to aircraft measurement altitudes.

We also consider temporal sensitivity patterns to compare the two LSM schemes. Figure 12 shows the diurnal distribution of biomass burning, and weekday and weekend anthropogenic BC emission sensitivities for both of the LSM configurations, and for unity weights, $w_k = 1$ and w_k from Eq. (27). Each bar in that plot represents a summation of sensitivities across the whole domain from 20 June, 00:00:00 UTC to 26 June,

GMDD
8, 2313–2367, 2015

23:00:00 UTC ($d = [1, \ldots, 7]$) within a particular local hour, n, such that

$$\frac{\partial \ln J}{\partial \ln E_n} = \sum_{i=1}^{n_x} \sum_{j=1}^{n_y} \sum_{d=1}^{7} \frac{\partial \ln J}{\partial \ln E_{i,j,d,n}}. \tag{30}$$

The signs and magnitudes of sensitivities fit the previous description for the spatially distributed temporal aggregation. The time period of emissions to which an observation is most sensitive depends on the altitude of that observation and the flow mechanisms that transport emitted aerosol mass to that observation. Thus, any conclusions drawn could be biased if observations do not have full temporal coverage, especially near sources. Since normalized sensitivities are proportional to emissions, it is to be expected that sensitivities at peak emission hours are magnified. Also, each hour of sensitivity is a sum of many diverse source locations. So while the net sensitivity in a single hour may be positive, the spatial distribution of sensitivities is much more varied, as was previously discussed.

The FINN biomass burning inventory applies an identical diurnal emission apportionment for all fires, regardless of vegetation, shading due to slopes, wind speed, or relative humidity. This scaling is applied in preprocessing. Both the PX and SLAB LSM setups seem to agree that the timing of the FINN burning emissions peak is correct within ±1 h and that the peak should be sharper. Without the weighting scheme, the PX configuration indicates that burning emissions are too low in peak hours, while the SLAB configuration concludes that burning emissions are too high in off-peak hours. With the weighting scheme applied, both configurations agree that fire emissions need to be increased to reduce the cost function. The increased burning sensitivity magnitudes indicate the weighting scheme is successful at generating a cost function that is more robustly sensitive to emission perturbations. The relative disagreement in sensitivity magnitude between the two LSM configurations is attributable to differences in residual errors, r_k, and the resulting adjoint forcings, $\lambda^*_{k,o}$. Both configurations seem to agree that the timing of emissions is correct, and in fact the midday peak should be

GMDD
8, 2313–2367, 2015

sharpened. However, the normalized sensitivities are proportional to emissions, meaning an emission peak should correspond to a sensitivity peak. Some work still needs to be done to interpret diurnal sensitivity patterns for use in a full inversion.

In contrast to FINN, NEI applies a variety of diurnal patterns to point, area, and traffic sources. The weekend and weekday emission profiles shown in Fig. 12 are the emission weighted averages for the entire domain. Individual sources may have a profile closer to flat, or alternatively zero overnight, and flat during daylight hours. The weighted average profile shown is close to the one used for commercial diesel traffic, since that is the largest BC source within the domain. Attributing sensitivities, or errors, to specific sectors is not straight-forward and doing so may require a smaller horizontal grid spacing to reduce the number of sectors per grid cell. Results for the weighted and unweighted cost functions are very similar. In general, anthropogenic emissions are too high throughout all times of the day on both weekdays and weekends. Both LSM configurations indicate the weekday profile peak should be sharper near 14:00 LT, and not at 16:00 LT, but also that emissions from 06:00 to 16:00 LT should be closer to the late evening and early morning magnitudes. The weekend sensitivities indicate the evening and morning emissions are too high, and that the daytime peak is timed about right, with the exception of the 18:00 LT spike. However, the relatively small magnitude of weekend sensitivities could also indicate there were not enough observations of anthropogenic sources on 21 June (SAT) and 22 (SUN) to draw definitive conclusions about emission timing.

Results for the two LSM options reveal the potential for model configuration to introduce bias in a 4D-Var inversion. For these particular observations, the posterior emissions from the PX option would likely be higher than those from the SLAB option, because of their relative sensitivity values. Model variability must be taken into consideration in 4D-Var sensitivity studies of high resolution emissions, because model variation represents a large fractional contribution to observation error variance for positive residuals, as shown in Fig. 9.

GMDD
8, 2313–2367, 2015

6 Conclusions

We have implemented, verified, and demonstrated the WRFPLUS-Chem coupled meteorology and chemical adjoint and tangent linear models for PBL mixing, emission, aging, dry deposition, and advection of BC aerosol. A second order checkpointing scheme enables tangent linear and adjoint model runs longer than six hours. The adjoint was used in the first iteration of a 4D-Var inversion within WRFDA-Chem, where model-observation residual errors are compared for low- and high-temporal resolution IMPROVE surface and ARCTAS-CARB aircraft observations during one week of June 2008. A novel cost function weighting scheme was devised to increase the impact of high significance observations in future 4D-Var inversions. Results indicate that the weighting scheme is effective at generating robust sensitivities of the cost function to emissions. The adjoint sensitivities also indicate that anthropogenic emissions are over predicted and burning emissions are under predicted for the domain and time period considered. The diurnal sensitivities would seem to indicate that burning emission profiles should be steeper midday, while anthropogenic emission profiles should be flattened on weekdays and sharpened on weekends. A full inversion is necessary to quantify the magnitude of the errors in the emissions. Additionally, adjoint sensitivities found using two different LSM options indicate that the results of such inversions will be sensitive to the choice of model configuration.

The next steps are as follows. We intend to incorporate tangent linear and adjoint observation operators for useful remote sensing products (e.g., aerosol optical depth (Saide et al., 2013) and absorbing aerosol optical depth). This addition will enable WRFDA-Chem to be applied to a wider range of domains and time periods and operationally. The WRFDA-Chem optimization algorithm still needs to be applied to control variables for chemical species initial conditions and emission scaling factors. Future development and incorporation of radiation and microphysics adjoints (e.g. Saide et al., 2012) will provide coupling between aerosols and meteorology, and provide new insights into sensitivities of direct, indirect, and semi-direct radiative forcing to emission

GMDD
8, 2313–2367, 2015

sectors and locations. In addition to the aerosol applications discussed, WRFDA-Chem 4D-Var will also be suited to emission inversions for green house gases and other chemical tracers.

The Supplement related to this article is available online at doi:10.5194/gmdd-8-2313-2015-supplement.

Acknowledgements. This research has been supported by a grant from the U.S. Environmental Protection Agency's Science to Achieve Results (STAR) program. Although the research described in the article has been funded wholly or in part by the U.S. Environmental Protection Agency's STAR program through grant R835037, it has not been subjected to any EPA review and therefore does not necessarily reflect the views of the Agency, and no official endorsement should be inferred. We are thankful for the ARCTAS mission, which was supported by NASA. We thank Y. Kondo for making the SP2 observations available through the NASA LaRC Airborne Science Data for Atmospheric Composition database. We acknowledge the use of FIRMS data from the Land Atmosphere Near-real time Capability for EOS (LANCE) system operated by the NASA/GSFC/Earth Science Data and Information System (ESDIS) with funding provided by NASA/HQ.

References

Al-Saadi, J., Soja, A. J., Pierce, R. B., Szykman, J., Wiedinmyer, C., Emmons, L., Kondragunta, S., Zhang, X., Kittaka, C., Schaack, T., and Bowman, K.: Intercomparison of near-real-time biomass burning emissions estimates constrained by satellite fire data, J. Appl. Remote Sens., 2, 021504, 1–24, doi:10.1117/1.2948785, 2008. 2331

Anenberg, S. C., Talgo, K., Arunachalam, S., Dolwick, P., Jang, C., and West, J. J.: Impacts of global, regional, and sectoral black carbon emission reductions on surface air quality and human mortality, Atmos. Chem. Phys., 11, 7253–7267, doi:10.5194/acp-11-7253-2011, 2011. 2317

Baklanov, A., Schlünzen, K., Suppan, P., Baldasano, J., Brunner, D., Aksoyoglu, S., Carmichael, G., Douros, J., Flemming, J., Forkel, R., Galmarini, S., Gauss, M., Grell, G.,

Hirtl, M., Joffre, S., Jorba, O., Kaas, E., Kaasik, M., Kallos, G., Kong, X., Korsholm, U., Kurganskiy, A., Kushta, J., Lohmann, U., Mahura, A., Manders-Groot, A., Maurizi, A., Moussiopoulos, N., Rao, S. T., Savage, N., Seigneur, C., Sokhi, R. S., Solazzo, E., Solomos, S., Sørensen, B., Tsegas, G., Vignati, E., Vogel, B., and Zhang, Y.: Online coupled regional meteorology chemistry models in Europe: current status and prospects, Atmos. Chem. Phys., 14, 317–398, doi:10.5194/acp-14-317-2014, 2014. 2315

Barker, D., Lee, M.-S., Guo, Y.-R., Huang, W., Huang, H., and Rizvi, Q.: WRF-Var – a unified 3/4D-Var variational data assimilation system for WRF, in: Sixth WRF/15th MM5 Users' Workshop, Boulder, CO, NCAR, 17 pp., available at: http://www2.mmm.ucar.edu/wrf/users/workshops/WS2005/presentations/session10/1-Barker.pdf (last access: 20 February 2015), 2005. 2316

Barker, D. M., Huang, W., Guo, Y.-R., Bourgeois, A. J., and Xiao, Q. N.: A three-dimensional variational data assimilation system for MM5: implementation and initial results, Mon. Weather Rev., 132, 897–914, 2004. 2316

Benedetti, A., Morcrette, J.-J., Boucher, O., Dethof, A., Engelen, R. J., Fisher, M., Flentje, H., Huneeus, N., Jones, L., Kaiser, J. W., Kinne, S., Mangold, A., Razinger, M., Simmons, A. J., and Suttie, M.: Aerosol analysis and forecast in the European Centre for Medium-Range Weather Forecasts Integrated Forecast System: 2. Data assimilation, J. Geophys. Res., 114, D13205, doi:10.1029/2008JD011115, 2009. 2316

Bond, T. C., Doherty, S. J., Fahey, D. W., Forster, P. M., Berntsen, T., DeAngelo, B. J., Flanner, M. G., Ghan, S., Kärcher, B., Koch, D., Kinne, S., Kondo, Y., Quinn, P. K., Sarofim, M. C., Schultz, M. G., Schulz, M., Venkataraman, C., Zhang, H., Zhang, S., Bellouin, N., Guttikunda, S. K., Hopke, P. K., Jacobson, M. Z., Kaiser, J. W., Klimont, Z., Lohmann, U., Schwarz, J. P., Shindell, D., Storelvmo, T., Warren, S. G., and Zender, C. S.: Bounding the role of black carbon in the climate system: a scientific assessment: black carbon in the climate system, J. Geophys. Res.-Atmos., 118, 5380–5552, doi:10.1002/jgrd.50171, 2013. 2317

Chin, M., Savoie, D. L., Huebert, B. J., Bandy, A. R., Thornton, D. C., Bates, T. S., Quinn, P. K., Saltzman, E. S., and De Bruyn, W. J.: Atmospheric sulfur cycle simulated in the global model GOCART: comparison with field observations and regional budgets, J. Geophys. Res.-Atmos., 105, 24689–24712, doi:10.1029/2000JD900385, 2000. 2323

Courtier, P., Thépaut, J.-N., and Hollingsworth, A.: A strategy for operational implementation of 4D-Var, using an incremental approach, Q. J. Roy. Meteor. Soc., 120, 1367–1387, doi:10.1002/qj.49712051912, 1994. 2319, 2321

Dubovik, O., Lapyonok, T., Kaufman, Y. J., Chin, M., Ginoux, P., Kahn, R. A., and Sinyuk, A.: Retrieving global aerosol sources from satellites using inverse modeling, Atmos. Chem. Phys., 8, 209–250, doi:10.5194/acp-8-209-2008, 2008. 2316

Flemming, J., Inness, A., Flentje, H., Huijnen, V., Moinat, P., Schultz, M. G., and Stein, O.: Coupling global chemistry transport models to ECMWF's integrated forecast system, Geosci. Model Dev., 2, 253–265, doi:10.5194/gmd-2-253-2009, 2009. 2315

Freitas, S. R., Longo, K. M., Chatfield, R., Latham, D., Silva Dias, M. A. F., Andreae, M. O., Prins, E., Santos, J. C., Gielow, R., and Carvalho Jr., J. A.: Including the sub-grid scale plume rise of vegetation fires in low resolution atmospheric transport models, Atmos. Chem. Phys., 7, 3385–3398, doi:10.5194/acp-7-3385-2007, 2007. 2331

Freitas, S. R., Longo, K. M., Trentmann, J., and Latham, D.: Technical Note: Sensitivity of 1-D smoke plume rise models to the inclusion of environmental wind drag, Atmos. Chem. Phys., 10, 585–594, doi:10.5194/acp-10-585-2010, 2010. 2331

Freitas, S. R., Longo, K. M., Alonso, M. F., Pirre, M., Marecal, V., Grell, G., Stockler, R., Mello, R. F., and Sánchez Gácita, M.: PREP-CHEM-SRC – 1.0: a preprocessor of trace gas and aerosol emission fields for regional and global atmospheric chemistry models, Geosci. Model Dev., 4, 419–433, doi:10.5194/gmd-4-419-2011, 2011. 2324

Giering, R. and Kaminski, T.: Recipes for adjoint code construction, ACM T. Math. Software, 24, 437–474, doi:10.1145/293686.293695, 1998. 2322

Grahame, T. J., Klemm, R., and Schlesinger, R. B.: Public health and components of particulate matter: the changing assessment of black carbon, J. Air Waste Manage., 64, 620–660, doi:10.1080/10962247.2014.912692, 2014. 2317

Grell, G., Freitas, S. R., Stuefer, M., and Fast, J.: Inclusion of biomass burning in WRF-Chem: impact of wildfires on weather forecasts, Atmos. Chem. Phys., 11, 5289–5303, doi:10.5194/acp-11-5289-2011, 2011. 2331

Grell, G. A. and Freitas, S. R.: A scale and aerosol aware stochastic convective parameterization for weather and air quality modeling, Atmos. Chem. Phys., 14, 5233–5250, doi:10.5194/acp-14-5233-2014, 2014. 2323

Grell, G. A., Knoche, R., Peckham, S. E., and McKeen, S. A.: Online versus offline air quality modeling on cloud-resolving scales, Geophys. Res. Lett., 31, L16117, doi:10.1029/2004GL020175, 2004. 2315

Grell, G. A., Peckham, S. E., Schmitz, R., McKeen, S. A., Frost, G., Skamarock, W. C., and Eder, B.: Fully coupled "online" chemistry within the WRF model, Atmos. Environ., 39, 6957–6975, 2005. 2315

Gumley, L.: MODIS Today, Space Science and Engineering Center, University of Wisconsin-Madison, Madison, WI, USA, available at: http://ge.ssec.wisc.edu/modis-today (last access: 20 January 2015), 2008. 2331

Hakami, A., Henze, D. K., Seinfeld, J. H., Chai, T., Tang, Y., Carmichael, G. R., and Sandu, A.: Adjoint inverse modeling of black carbon during the Asian Pacific Regional Aerosol Characterization Experiment, J. Geophys. Res.-Atmos., 110, D14301, doi:10.1029/2004JD005671, 2005. 2316

Hansen, J., Sato, M., and Ruedy, R.: Radiative forcing and climate response, J. Geophys. Res.-Atmos., 102, 6831–6864, doi:10.1029/96JD03436, 1997. 2315

Hansen, M., DeFries, R., Townshend, J., Carroll, M., Dimiceli, C., and Sohlberg, R.: 500 m MODIS Vegetation Continuous Fields, The Global Land Cover Facility, College Park, Maryland, 2003. 2330

Hascoët, L. and Pascual, V.: The Tapenade Automatic Differentiation tool: principles, model, and specification, ACM T. Math. Software, 39, 20, 1–43, doi:10.1145/2450153.2450158, 2013. 2322

Henze, D. K., Hakami, A., and Seinfeld, J. H.: Development of the adjoint of GEOS-Chem, Atmos. Chem. Phys., 7, 2413–2433, doi:10.5194/acp-7-2413-2007, 2007. 2316, 2325

Henze, D. K., Seinfeld, J. H., and Shindell, D. T.: Inverse modeling and mapping US air quality influences of inorganic $PM_{2.5}$ precursor emissions using the adjoint of GEOS-Chem, Atmos. Chem. Phys., 9, 5877–5903, doi:10.5194/acp-9-5877-2009, 2009. 2316

Huang, X.-Y., Xiao, Q., Barker, D. M., Zhang, X., Michalakes, J., Huang, W., Henderson, T., Bray, J., Chen, Y., Ma, Z., Dudhia, J., Guo, Y., Zhang, X., Won, D.-J., Lin, H.-C., and Kuo, Y.-H.: Four-dimensional variational data assimilation for WRF: formulation and preliminary results, Mon. Weather Rev., 137, 299–314, doi:10.1175/2008MWR2577.1, 2009. 2316, 2320, 2321

Huneeus, N., Boucher, O., and Chevallier, F.: Simplified aerosol modeling for variational data assimilation, Geosci. Model Dev., 2, 213–229, doi:10.5194/gmd-2-213-2009, 2009. 2316

Inness, A., Baier, F., Benedetti, A., Bouarar, I., Chabrillat, S., Clark, H., Clerbaux, C., Coheur, P., Engelen, R. J., Errera, Q., Flemming, J., George, M., Granier, C., Hadji-Lazaro, J., Huijnen, V., Hurtmans, D., Jones, L., Kaiser, J. W., Kapsomenakis, J., Lefever, K., Leitão, J.,

Razinger, M., Richter, A., Schultz, M. G., Simmons, A. J., Suttie, M., Stein, O., Thépaut, J.-N., Thouret, V., Vrekoussis, M., Zerefos, C., and the MACC team: The MACC reanalysis: an 8 yr data set of atmospheric composition, Atmos. Chem. Phys., 13, 4073–4109, doi:10.5194/acp-13-4073-2013, 2013. 2316

Jacob, D. J., Crawford, J. H., Maring, H., Clarke, A. D., Dibb, J. E., Emmons, L. K., Ferrare, R. A., Hostetler, C. A., Russell, P. B., Singh, H. B., Thompson, A. M., Shaw, G. E., McCauley, E., Pederson, J. R., and Fisher, J. A.: The Arctic Research of the Composition of the Troposphere from Aircraft and Satellites (ARCTAS) mission: design, execution, and first results, Atmos. Chem. Phys., 10, 5191–5212, doi:10.5194/acp-10-5191-2010, 2010. 2331

Kaminski, J. W., Neary, L., Struzewska, J., McConnell, J. C., Lupu, A., Jarosz, J., Toyota, K., Gong, S. L., Côté, J., Liu, X., Chance, K., and Richter, A.: GEM-AQ, an on-line global multiscale chemical weather modelling system: model description and evaluation of gas phase chemistry processes, Atmos. Chem. Phys., 8, 3255–3281, doi:10.5194/acp-8-3255-2008, 2008. 2315

Kinnison, D. E., Brasseur, G. P., Walters, S., Garcia, R. R., Marsh, D. R., Sassi, F., Harvey, V. L., Randall, C. E., Emmons, L., Lamarque, J. F., Hess, P., Orlando, J. J., Tie, X. X., Randel, W., Pan, L. L., Gettelman, A., Granier, C., Diehl, T., Niemeier, U., and Simmons, A. J.: Sensitivity of chemical tracers to meteorological parameters in the MOZART-3 chemical transport model, J. Geophys. Res., 112, D20302, doi:10.1029/2006JD007879, 2007. 2315

Koch, D. and Del Genio, A. D.: Black carbon semi-direct effects on cloud cover: review and synthesis, Atmos. Chem. Phys., 10, 7685–7696, doi:10.5194/acp-10-7685-2010, 2010. 2315

Kondo, Y., Sahu, L., Moteki, N., Khan, F., Takegawa, N., Liu, X., Koike, M., and Miyakawa, T.: Consistency and traceability of black carbon measurements made by laser-induced incandescence, thermal-optical transmittance, and filter-based photo-absorption techniques, Aerosol Sci. Tech., 45, 295–312, doi:10.1080/02786826.2010.533215, 2011. 2335

Krewski, D., Jerrett, M., Burnett, R. T., Ma, R., Hughes, E., Shi, Y., Turner, M. C., Pope III, C. A., Thurston, G., Calle, E. E., and Eugenia, E.: Extended Follow-Up and Spatial Analysis of the American Cancer Society Study Linking Particulate Air Pollution and Mortality, Tech. Rep. 140, Health Effects Institute, available at: http://www.healtheffects.org/Pubs/RR140-Krewski.pdf (last access: 15 August 2014), 2009. 2314

Liu, Z., Liu, Q., Lin, H.-C., Schwartz, C. S., Lee, Y.-H., and Wang, T.: Three-dimensional variational assimilation of MODIS aerosol optical depth: implementation and application to a dust

GMDD
8, 2313–2367, 2015

storm over East Asia: AOD DATA ASSIMILATION, J. Geophys. Res.-Atmos., 116, D23206, doi:10.1029/2011JD016159, 2011. 2315

Lohmann, U. and Feichter, J.: Global indirect aerosol effects: a review, Atmos. Chem. Phys., 5, 715–737, doi:10.5194/acp-5-715-2005, 2005. 2315

Malm, W. C., Sisler, J. F., Huffman, D., Eldred, R. A., and Cahill, T. A.: Spatial and seasonal trends in particle concentration and optical extinction in the United States, J. Geophys. Res.-Atmos., 99, 1347–1370, doi:10.1029/93JD02916, 1994. 2331

Morcrette, J.-J., Boucher, O., Jones, L., Salmond, D., Bechtold, P., Beljaars, A., Benedetti, A., Bonet, A., Kaiser, J. W., Razinger, M., Schulz, M., Serrar, S., Simmons, A. J., Sofiev, M., Suttie, M., Tompkins, A. M., and Untch, A.: Aerosol analysis and forecast in the European Centre for Medium-Range Weather Forecasts Integrated Forecast System: forward modeling, J. Geophys. Res., 114, D06206, doi:10.1029/2008JD011235, 2009. 2315

Myhre, G., Shindell, D., Breon, F., Collins, W., Fuglestvedt, J., Huang, J., Koch, D., Lamarque, J., Lee, D., Mendoza, B., Nakajima, T., Robock, A., Stephens, G., Takemura, T., and Zhang, H.: Anthropogenic and natural radiative forcing, in: Climate Change 2013: The Physical Science Basis. Contribution of Working Group I to the Fifth Assessment Report of the Intergovernmental Panel on Climate Change, edited by: Stocker, T. F., Qin, D., Plattner, G.-K., Tignor, M., Allen, S. K., Boschung, J., Nauels, A., Xia, Y., Bex, V., and Midgley, P. M., Cambridge University Press, Cambridge, UK and New York, NY, USA, 129–234, 2013. 2314

NASA: MCD14ML MODIS Active Fire Detections, available at: https://earthdata.nasa.gov/active-fire-data#tab-content-6, last access: 18 December 2014. 2331

Pagowski, M. and Grell, G. A.: Experiments with the assimilation of fine aerosols using an ensemble Kalman filter, J. Geophys. Res.-Atmos., 117, D21302, doi:10.1029/2012JD018333, 2012. 2315

Pagowski, M., Grell, G. A., McKeen, S. A., Peckham, S. E., and Devenyi, D.: Three-dimensional variational data assimilation of ozone and fine particulate matter observations: some results using the Weather Research and forecasting-chemistry model and grid-point statistical interpolation, Q. J. Roy. Meteor. Soc., 136, 2013–2024, doi:10.1002/qj.700, 2010. 2315

Pleim, J. E.: A simple, efficient solution of flux–profile relationships in the atmospheric surface layer, J. Appl. Meteorol. Clim., 45, 341–347, doi:10.1175/JAM2339.1, 2006. 2319

Pleim, J. E.: A combined local and nonlocal closure model for the atmospheric boundary layer. Part I: Model description and testing, J. Appl. Meteorol. Clim., 46, 1383–1395, doi:10.1175/JAM2539.1, 2007a. 2319

Pleim, J. E.: A combined local and nonlocal closure model for the atmospheric boundary layer. Part II: Application and evaluation in a mesoscale meteorological model, J. Appl. Meteorol. Clim., 46, 1396–1409, doi:10.1175/JAM2534.1, 2007b. 2319

Pleim, J. E. and Gilliam, R.: An indirect data assimilation scheme for deep soil temperature in the Pleim–Xiu Land Surface Model, J. Appl. Meteorol. Clim., 48, 1362–1376, doi:10.1175/2009JAMC2053.1, 2009. 2319

Pleim, J. E. and Xiu, A.: Development of a land surface model. Part II: Data assimilation, J. Appl. Meteorol., 42, 1811–1822, 2003. 2319

Sahu, L. K., Kondo, Y., Moteki, N., Takegawa, N., Zhao, Y., Cubison, M. J., Jimenez, J. L., Vay, S., Diskin, G. S., Wisthaler, A., Mikoviny, T., Huey, L. G., Weinheimer, A. J., and Knapp, D. J.: Emission characteristics of black carbon in anthropogenic and biomass burning plumes over California during ARCTAS-CARB 2008, J. Geophys. Res., 117, D16302, doi:10.1029/2011JD017401, 2012. 2331, 2335

Saide, P. E., Carmichael, G. R., Spak, S. N., Minnis, P., and Ayers, J. K.: Improving aerosol distributions below clouds by assimilating satellite-retrieved cloud droplet number, P. Natl. Acad. Sci. USA, 109, 11939–11943, available at: http://www.pnas.org/content/109/30/11939.short (last access: 16 August 2014), 2012. 2315, 2319, 2345

Saide, P. E., Carmichael, G. R., Liu, Z., Schwartz, C. S., Lin, H. C., da Silva, A. M., and Hyer, E.: Aerosol optical depth assimilation for a size-resolved sectional model: impacts of observationally constrained, multi-wavelength and fine mode retrievals on regional scale analyses and forecasts, Atmos. Chem. Phys., 13, 10425–10444, doi:10.5194/acp-13-10425-2013, 2013. 2315, 2319, 2345

Samset, B. H., Myhre, G., Schulz, M., Balkanski, Y., Bauer, S., Berntsen, T. K., Bian, H., Bellouin, N., Diehl, T., Easter, R. C., Ghan, S. J., Iversen, T., Kinne, S., Kirkevåg, A., Lamarque, J.-F., Lin, G., Liu, X., Penner, J. E., Seland, Ø., Skeie, R. B., Stier, P., Takemura, T., Tsigaridis, K., and Zhang, K.: Black carbon vertical profiles strongly affect its radiative forcing uncertainty, Atmos. Chem. Phys., 13, 2423–2434, doi:10.5194/acp-13-2423-2013, 2013. 2315

Sandu, A., Daescu, D. N., Carmichael, G. R., and Chai, T.: Adjoint sensitivity analysis of regional air quality models, J. Comput. Phys., 204, 222–252, doi:10.1016/j.jcp.2004.10.011, 2005. 2316

Schulz, M., Textor, C., Kinne, S., Balkanski, Y., Bauer, S., Berntsen, T., Berglen, T., Boucher, O., Dentener, F., Guibert, S., Isaksen, I. S. A., Iversen, T., Koch, D., Kirkevåg, A., Liu, X., Monta-

naro, V., Myhre, G., Penner, J. E., Pitari, G., Reddy, S., Seland, Ø., Stier, P., and Takemura, T.: Radiative forcing by aerosols as derived from the AeroCom present-day and pre-industrial simulations, Atmos. Chem. Phys., 6, 5225–5246, doi:10.5194/acp-6-5225-2006, 2006. 2315

Schwartz, C. S., Liu, Z., Lin, H.-C., and McKeen, S. A.: Simultaneous three-dimensional variational assimilation of surface fine particulate matter and MODIS aerosol optical depth, J. Geophys. Res., 117, D13202, doi:10.1029/2011JD017383, 2012. 2315

Schwartz, C. S., Liu, Z., Lin, H.-C., and Cetola, J. D.: Assimilating aerosol observations with a "hybrid" variational-ensemble data assimilation system, J. Geophys. Res.-Atmos., 119, 4043–4069, doi:10.1002/2013JD020937, 2014. 2315

Schwartz, J., Coull, B., Laden, F., and Ryan, L.: The effect of dose and timing of dose on the association between airborne particles and survival, Environ. Health Persp., 116, 64–69, doi:10.1289/ehp.9955, 2007. 2314

Skamarock, W. C., Klemp, J. B., Dudhia, J., Gill, D. O., Barker, D. M., Duda, M. G., Huang, X.-Y., Wang, W., and Powers, J. G.: A description of the advanced research WRF version 3, Tech. rep., DTIC Document, available at: http://nldr.library.ucar.edu/repository/collections/TECH-NOTE-000-000-000-855 (last access: 28 January 2014), 2008. 2315

Streets, D. G., Bond, T. C., Carmichael, G. R., Fernandes, S. D., Fu, Q., He, D., Klimont, Z., Nelson, S. M., Tsai, N. Y., Wang, M. Q., Woo, J.-H., and Yarber, K. F.: An inventory of gaseous and primary aerosol emissions in Asia in the year 2000, J. Geophys. Res.-Atmos., 108, D20, GTE30/1–GTE30/23, doi:10.1029/2002JD003093, 2003. 2315

Suutari, R., Amann, M., Cofala, J., Klimont, Z., Posch, M., and Schöpp, W.: From economic activities to ecosystem protection in Europe – an uncertainty analysis of two scenarios of the RAINS integrated assessment model, Tech. Rep. CIAM/CCE Rep. 1/2001, Int. Inst. for Appl. Syst. Anal., Laxenburg, Austria, 2001. 2315

Textor, C., Schulz, M., Guibert, S., Kinne, S., Balkanski, Y., Bauer, S., Berntsen, T., Berglen, T., Boucher, O., Chin, M., Dentener, F., Diehl, T., Easter, R., Feichter, H., Fillmore, D., Ghan, S., Ginoux, P., Gong, S., Grini, A., Hendricks, J., Horowitz, L., Huang, P., Isaksen, I., Iversen, I., Kloster, S., Koch, D., Kirkevåg, A., Kristjansson, J. E., Krol, M., Lauer, A., Lamarque, J. F., Liu, X., Montanaro, V., Myhre, G., Penner, J., Pitari, G., Reddy, S., Seland, Ø., Stier, P., Takemura, T., and Tie, X.: Analysis and quantification of the diversities of aerosol life cycles within AeroCom, Atmos. Chem. Phys., 6, 1777–1813, doi:10.5194/acp-6-1777-2006, 2006. 2315

GMDD
8, 2313–2367, 2015

Turner, A. J., Henze, D. K., Martin, R. V., and Hakami, A.: The spatial extent of source influences on modeled column concentrations of short-lived species: modeled source influences, Geophys. Res. Lett., 39, L12806, doi:10.1029/2012GL051832, 2012. 2316

Turner, M., Henze, D., Hakami, A., Zhao, S., Resler, J., Carmichael, G., Stanier, C., Baek, J., Sandu, A., Russell, A., Jeong, G., Capps, S., Percell, P., Pinder, R., Napelenok, S., Bash, J., and Chai, T.: Differences between magnitudes and health impacts of BC emissions across the US using 12 km scale seasonal source apportionment, submitted, 2015. 2316

Twomey, S.: The influence of pollution on the shortwave Albedo of clouds, J. Atmos. Sci., 34, 1149–1152, doi:10.1175/1520-0469(1977)034<1149:TIOPOT>2.0.CO;2, 1977. 2315

UC-Davis: Interagency Monitoring of Protected Visual Environments Quality Assurance Project Plan, Tech. rep., available at: http://vista.cira.colostate.edu/improve/Publications/QA_QC/IMPROVE_QAPP_R0.pdf (last access: 16 November 2012), 2002. 2335

Vogel, B., Vogel, H., Bäumer, D., Bangert, M., Lundgren, K., Rinke, R., and Stanelle, T.: The comprehensive model system COSMO-ART – Radiative impact of aerosol on the state of the atmosphere on the regional scale, Atmos. Chem. Phys., 9, 8661–8680, doi:10.5194/acp-9-8661-2009, 2009. 2315

Wang, J., Xu, X., Henze, D. K., Zeng, J., Ji, Q., Tsay, S.-C., and Huang, J.: Top-down estimate of dust emissions through integration of MODIS and MISR aerosol retrievals with the GEOS-Chem adjoint model, Geophys. Res. Lett., 39, L08802, doi:10.1029/2012GL051136, 2012. 2316

Wesely, M. L.: Parameterization of surface resistances to gaseous dry deposition in regional-scale numerical models, Atmos. Environ., 23, 1293–1304, doi:10.1016/0004-6981(89)90153-4, 1989. 2319

Wiedinmyer, C., Quayle, B., Geron, C., Belote, A., McKenzie, D., Zhang, X., O'Neill, S., and Wynne, K. K.: Estimating emissions from fires in North America for air quality modeling, Atmos. Environ., 40, 3419–3432, doi:10.1016/j.atmosenv.2006.02.010, 2006. 2330

Wiedinmyer, C., Akagi, S. K., Yokelson, R. J., Emmons, L. K., Al-Saadi, J. A., Orlando, J. J., and Soja, A. J.: The Fire INventory from NCAR (FINN): a high resolution global model to estimate the emissions from open burning, Geosci. Model Dev., 4, 625–641, doi:10.5194/gmd-4-625-2011, 2011. 2330

Xiao, Q., Kuo, Y.-H., Ma, Z., Huang, W., Huang, X.-Y., Zhang, X., Barker, D. M., Michalakes, J., and Dudhia, J.: Application of an Adiabatic WRF Adjoint to the investigation of the

GMDD
8, 2313–2367, 2015

May 2004 McMurdo, Antarctica, severe wind event, Mon. Weather Rev., 136, 3696–3713, doi:10.1175/2008MWR2235.1, 2008. 2322

Xiu, A. and Pleim, J. E.: Development of a land surface model. Part I: Application in a mesoscale meteorological model, J. Appl. Meteorol., 40, 192–209, 2001. 2319

Zhang, X., Huang, X.-Y., and Pan, N.: Development of the upgraded tangent linear and adjoint of the weather research and forecasting (WRF) model, J. Atmos. Ocean. Tech., 30, 1180–1188, doi:10.1175/JTECH-D-12-00213.1, 2013. 2317, 2322, 2325

GMDD

8, 2313–2367, 2015

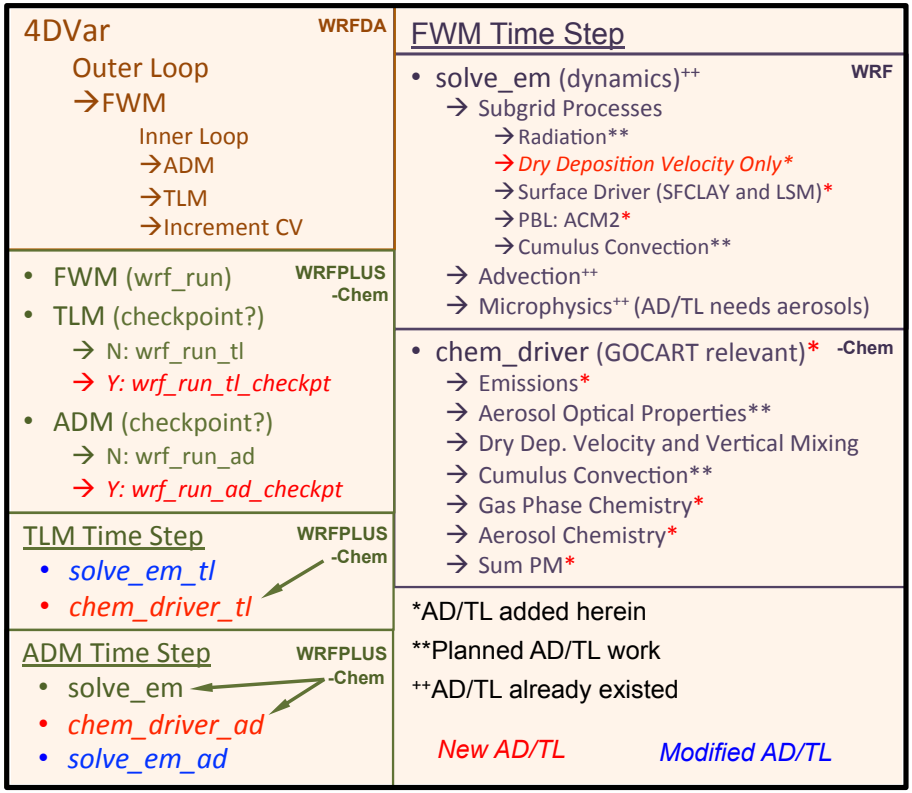

Figure 1. Dependencies between WRF, WRF-Chem, WRFPLUS AD/TL, and WRFDA. AD/TL development status is also noted.

GMDD
8, 2313–2367, 2015

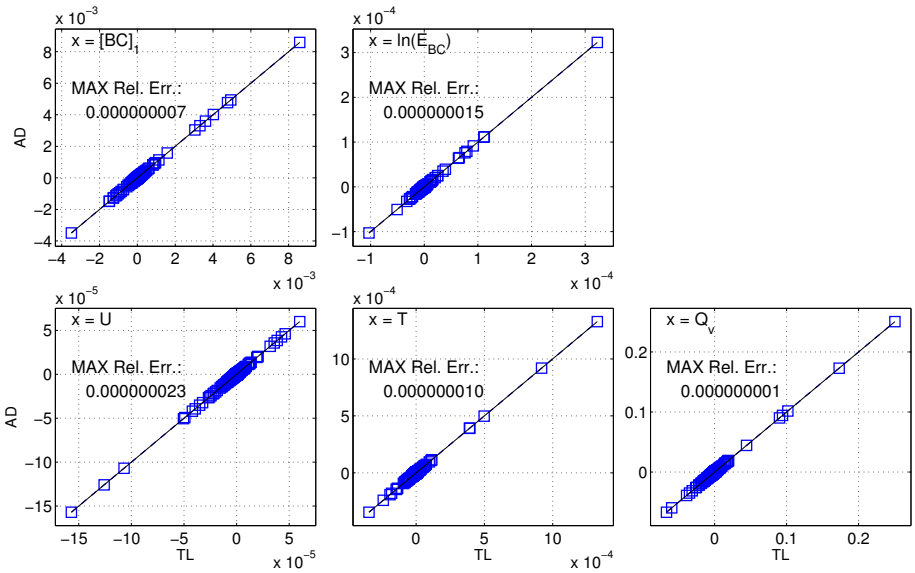

Figure 2. Comparison of ADM to TLM evaluations of $\frac{\partial[\mathrm{BC}_1]}{\partial x}$ and $\frac{\partial[\mathrm{BC}_2]}{\partial x}$ for 300 derivatives for each denominator variable.

GMDD
8, 2313–2367, 2015

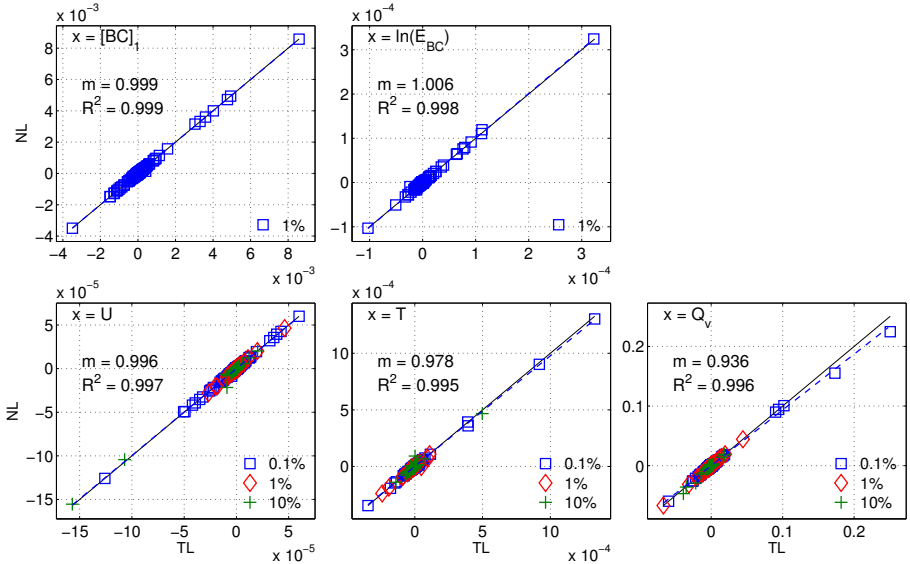

Figure 3. Comparison of nonlinear finite difference approximations to TLM evaluations of $\frac{\partial[\mathrm{BC}_1]}{\partial \boldsymbol{x}}$ and $\frac{\partial[\mathrm{BC}_2]}{\partial \boldsymbol{x}}$ for 300 derivatives for each denominator variable. The different markers for $\boldsymbol{x} = [U, T, Q_v]$ indicate the δx percentage that yielded a finite difference derivative closest to the tangent linear value.

GMDD
8, 2313–2367, 2015

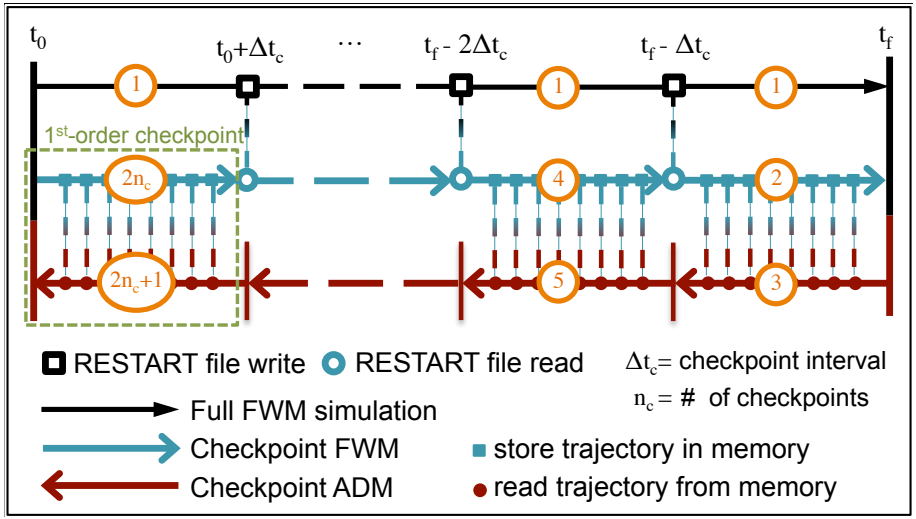

Figure 4. Second order checkpointing scheme implemented in WRFPLUS-Chem.

GMDD
8, 2313–2367, 2015

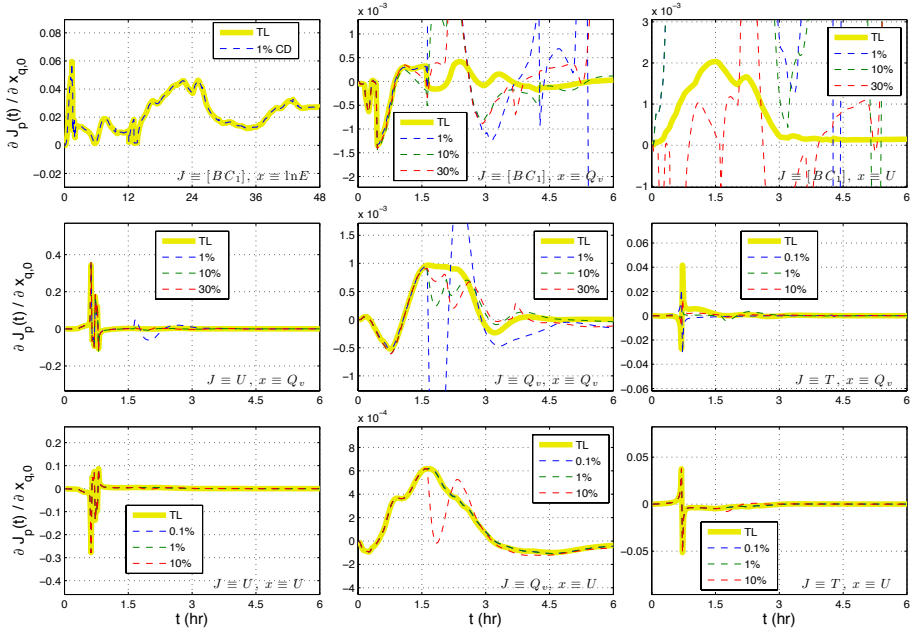

Figure 5. Time variant sensitivities of cost function J with respect to control variable x for multiple perturbations and the TLM with second order checkpointing.

GMDD
8, 2313–2367, 2015

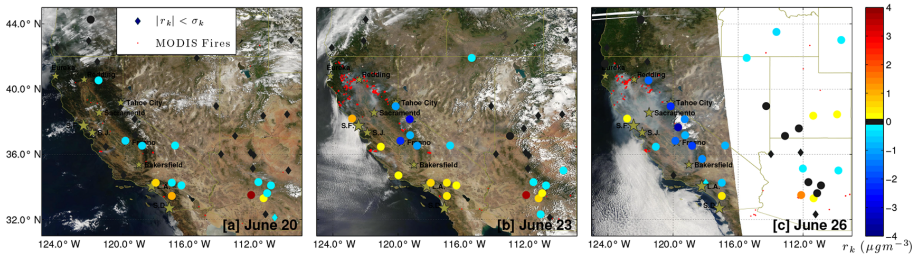

Figure 6. Surface site residual model error, r_k, overlaid on MODIS Aqua true color images and active fire retrievals. Observations with a bias less than one SD are also indicated.

GMDD
8, 2313–2367, 2015

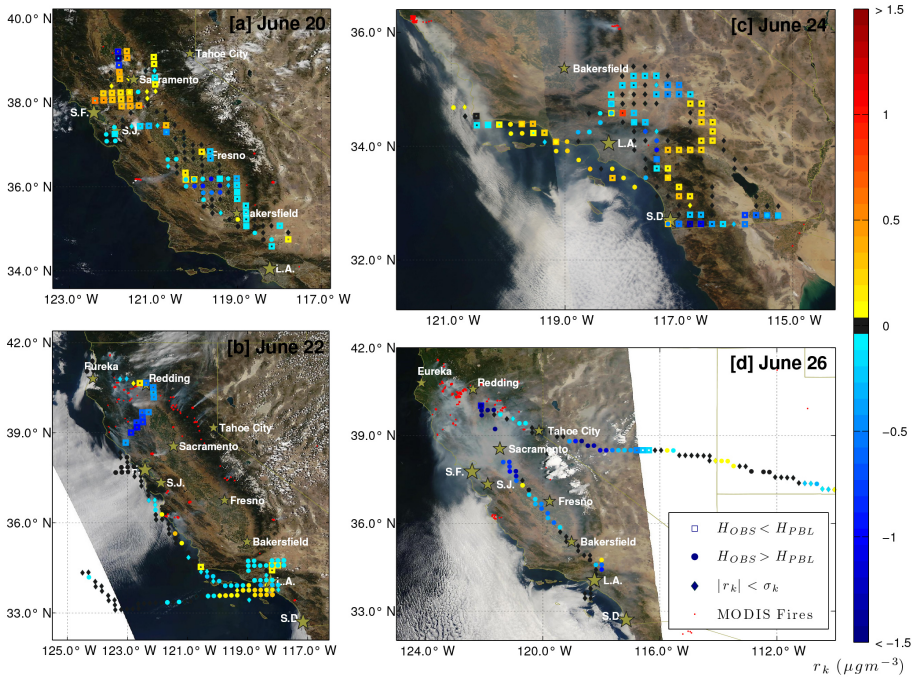

Figure 7. Aircraft residual model error, r_k, with indication for the observation height relative to the model PBL height overlaid on MODIS Aqua true color images and active fire retrievals. Observations with a bias less than one SD are also indicated.

GMDD
8, 2313–2367, 2015

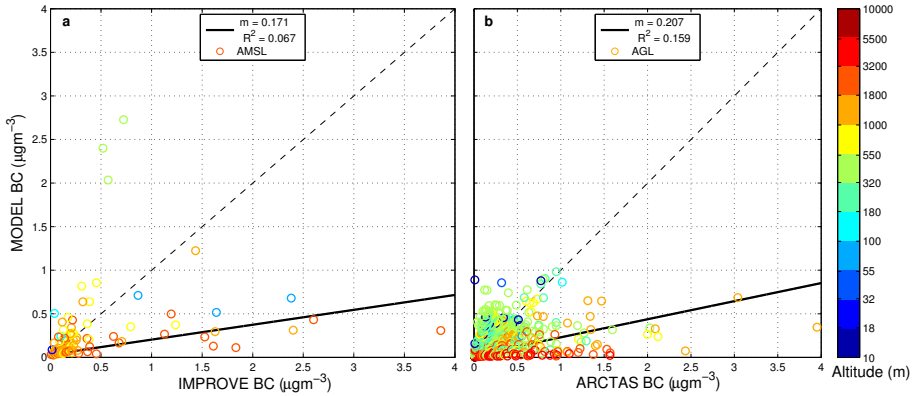

Figure 8. Linear fits between model BC concentrations with slope m and coefficient of determination R^2 for **(a)** IMPROVE surface and **(b)** ARCTAS-CARB aircraft observations colored by model height above mean sea level (a.m.s.l.) and above ground level (a.g.l.).

GMDD
8, 2313–2367, 2015

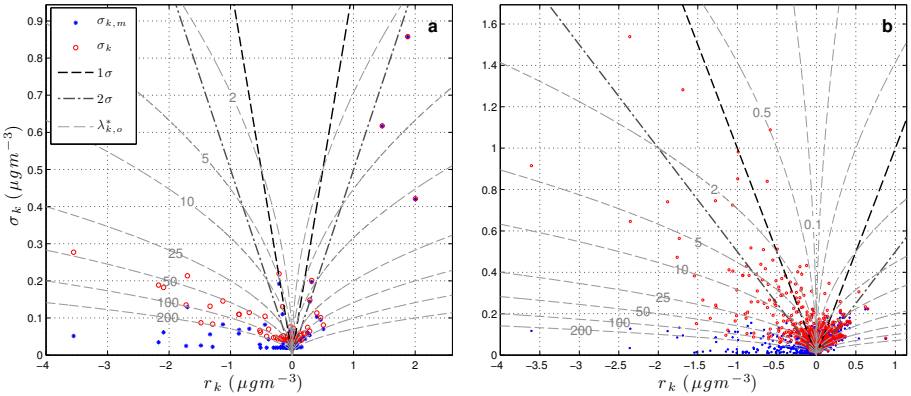

Figure 9. Model and total observation error SD ($\sigma_{k,m}, \sigma_k$) vs. model residual error (r_k) with adjoint forcing ($\lambda^*_{k,o}$) contours corresponding to $w_k = 1$ for **(a)** surface and **(b)** aircraft observations. 1σ and 2σ zones reflect regions of increasing statistical significance.

GMDD
8, 2313–2367, 2015

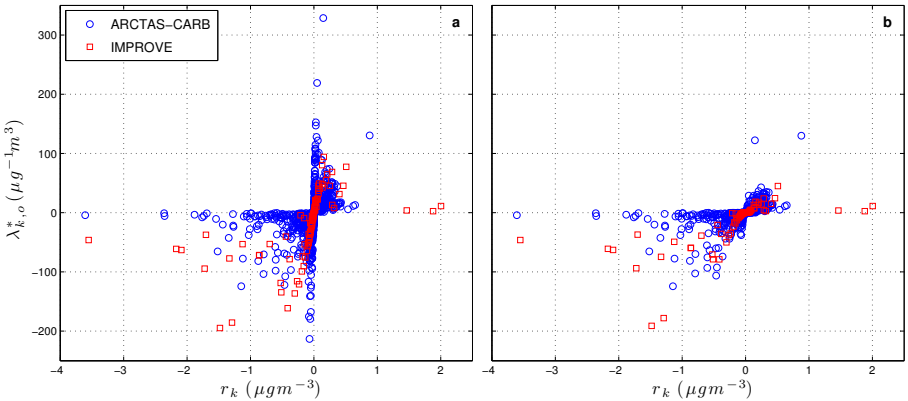

Figure 10. Adjoint forcing ($\lambda^*_{k,o}$) vs. residual error (r_k) for ARCTAS and IMPROVE observations using weights of **(a)** w_k =1 and **(b)** w_k from Eq. (27).

GMDD
8, 2313–2367, 2015

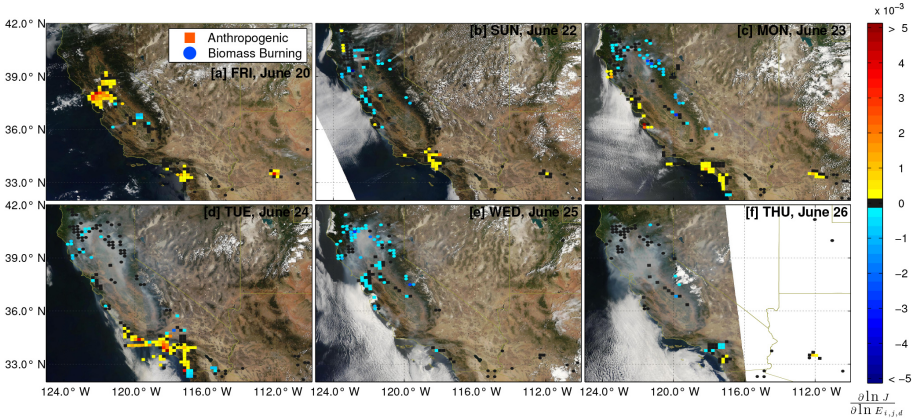

Figure 11. Normalized sensitivities ($\frac{\partial \ln J}{\partial \ln E_{i,j,d}}$) of the 4D-Var cost function (for surface and aircraft observations) with respect to anthropogenic and burning emission scaling factors overlaid on MODIS Aqua true color images for six days during the simulation. Anthropogenic sensitivities with magnitudes less than 1 % of the maximum anthropogenic sensitivity magnitude are removed. There is a marker for all grid cells with non-zero burning emissions.

GMDD
8, 2313–2367, 2015

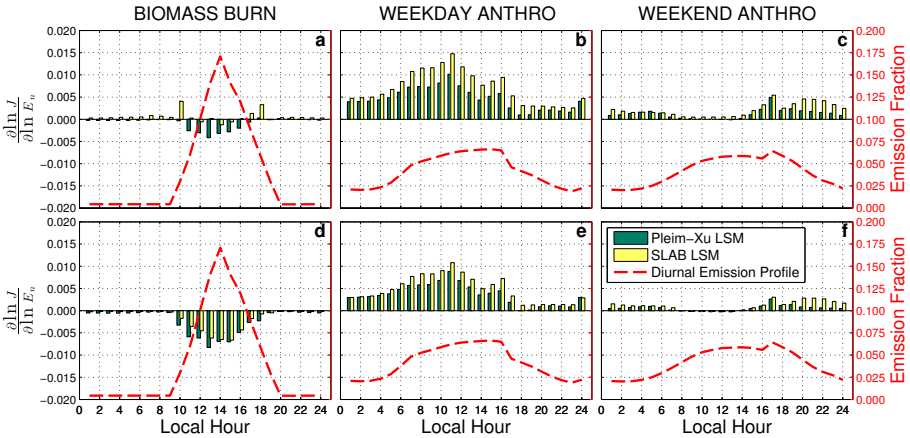

Figure 12. Diurnal normalized sensitivities ($\frac{\partial \ln J}{\partial \ln E_n}$) of the 4D-Var cost function with respect to emissions scaling factors for (**a**, **b**, and **c**) $w_k = 1$ and (**d**, **e**, and **f**) w_k from Eq. (27). Also plotted are diurnal emission fractions. Sensitivities were calculated for two different WRF LSM options and are shown separately for biomass burning, and weekend and weekday anthropogenic emissions.

GMDD
8, 2313–2367, 2015